Polydispersity effects in poly(isoprene-b-styrene-b-ethylene oxide) triblock terpolymers

Adam J. Meuler, Christopher J. Ellison, Jian Qin, Christopher M. Evans, Marc A. Hillmyer et al.

Citation: J. Chem. Phys. **130**, 234903 (2009); doi: 10.1063/1.3140205
View online: http://dx.doi.org/10.1063/1.3140205
View Table of Contents: http://jcp.aip.org/resource/1/JCPSA6/v130/i23
Published by the AIP Publishing LLC.

Polydispersity effects in poly(isoprene-*b*-styrene-*b*-ethylene oxide) triblock terpolymers

Adam J. Meuler,[1] Christopher J. Ellison,[1,b)] Jian Qin,[1] Christopher M. Evans,[1] Marc A. Hillmyer,[2,a)] and Frank S. Bates[1,a)]
[1]*Department of Chemical Engineering and Materials Science, University of Minnesota, Minneapolis, Minnesota 55455, USA*
[2]*Department of Chemistry, University of Minnesota, Minneapolis, Minnesota 55455, USA*

(Received 4 March 2009; accepted 24 April 2009; published online 17 June 2009)

Four hydroxyl-terminated poly(isoprene-*b*-styrene) diblock copolymers with comparable molecular weights and compositions (equivalent volume fractions of polyisoprene and polystyrene) but different polystyrene block polydispersity indices ($M_w/M_n=1.06, 1.16, 1.31, 1.44$) were synthesized by anionic polymerization using either *sec*-butyllithium or the functional organolithium 3-triisopropylsilyloxy-1-propyllithium. Poly(ethylene oxide) (PEO) blocks were grown from the end of each of these parent diblocks to yield four series of poly(isoprene-*b*-styrene-*b*-ethylene oxide) (ISO) triblock terpolymers that were used to interrogate the effects of varying the polydispersity of the middle bridged polystyrene block. In addition to the neat triblock samples, 13 multicomponent blends were prepared at four different compositions from the ISO materials containing a polystyrene segment with $M_w/M_n=1.06$; these blends were used to probe the effects of increasing the polydispersity of the terminal PEO block. The melt-phase behavior of all samples was characterized using small-angle X-ray scattering and dynamic mechanical spectroscopy. Numerous polydispersity-driven morphological transitions are reported, including transitions from lamellae to core-shell gyroid, from core-shell gyroid to hexagonally packed cylinders, and from network morphologies [either O^{70} (the orthorhombic *Fddd* network) or core-shell gyroid] to lamellae. Domain periodicities and order-disorder transition temperatures also vary with block polydispersities. Self-consistent field theory calculations were performed to supplement the experimental investigations and help elucidate the molecular factors underlying the polydispersity effects. The consequences of varying the polydispersity of the terminal PEO block are comparable to the polydispersity effects previously reported in AB diblock copolymers. Namely, domain periodicities increase with increasing polydispersity and domain interfaces tend to curve toward polydisperse blocks. The changes in phase behavior that are associated with variations in the polydispersity of the middle bridged polystyrene block, however, are not analogous to those reported in AB diblock copolymers, as increases in this middle block polydispersity are not always accompanied by (i) increased domain periodicities and (ii) a tendency for domain interfaces to curve toward the polydisperse domain. These results highlight the utility of polydispersity as a tool to tune the phase behavior of ABC block terpolymers. © *2009 American Institute of Physics*.
[DOI: 10.1063/1.3140205]

I. INTRODUCTION

Most research on block copolymers has focused on "model" macromolecules that contain nearly monodisperse (polydispersity index, PDI=$M_w/M_n<1.1$) blocks. These materials are typically prepared using living anionic polymerization, a methodology that has seen commercial success.[1] However, only a limited number of monomers and reaction sequences are amenable to living anionic polymerization, which may be prohibitively expensive.[2] To overcome these limitations, researchers have developed a variety of alternative synthetic strategies, such as chain shuttling polymerizations,[3,4] ring-opening metathesis polymerizations,[5] and controlled radical polymerizations.[6–9] While these methods increase the number of monomers that can be incorporated into block copolymers, possibly at lower costs, block PDIs greater than 1.2 often result.[10,11] Since many block copolymer properties are derived from the underlying morphology, understanding the effects of polydispersity on block copolymer phase behavior should hasten the implementation of polydisperse block copolymers in advanced material applications.

Although the potential significance of polydispersity effects was pointed out more than 25 years ago by Leibler,[12] few reports describing polydisperse materials appeared in the literature prior to 2002,[13–24] when Bendejacq *et al.*[10] showed that poly(styrene-*b*-acrylic acid) diblock copolymers with overall polydispersities near 2 formed well-ordered mesostructures. A flurry of theoretical[25–34] and

a)Authors to whom correspondence should be addressed: Electronic addresses: hillmyer@umn.edu and bates@cems.umn.edu.
b)Presently at Department of Chemical Engineering, University of Texas at Austin, Austin, TX 78712.

experimental[11,27,35–43] studies of polydispersity effects in AB block copolymers followed Bendejacq *et al.*'s report. This topic recently has been reviewed,[44] and only a brief summary is provided below.

Polydisperse AB diblock and ABA triblock materials generally adopt the familiar block copolymer mesostructures of lamellae (LAM), hexagonally packed cylinders (HEX), spheres packed on a body-centered cubic lattice (bcc), and gyroid (G).[26–28,30,31] Polydispersity does influence block copolymer phase behavior, however, as it affects order-disorder transition temperatures (T_{ODT}'s)[33,40,43] and can drive morphological transitions; the locations of the boundaries on the phase portrait depend on the polydispersities of the constituent A and B blocks.[26–28,30,31] Such morphological transitions have been attributed to changes in the average stretching energy that accompany the introduction of domain polydispersity.[28,30] The ensemble of chains in a polydisperse block does not have to stretch as much as its monodisperse counterpart to fill space, effectively lowering the stretching free energy of the block.[28,30] As a result, there is a tendency for the "softer" (polydisperse) block to stretch so that chains in the opposing monodisperse domain may relax; this process may drive morphological transitions in which the interfaces curve toward the polydisperse domain.[26–28,30] Morphologies with smaller mean interfacial curvatures are stabilized when the polydisperse block is the major component, while microstructures with larger mean interfacial curvatures are preferred when the minority block is polydisperse. The reduction in elastic free energy is also accompanied by an increase in the height of end-grafted polymer brushes[17] and an increase in the domain period in the melt.[27–29,31,33,35–37,43] Furthermore, the distribution of chain lengths present in polydisperse materials may stabilize additional ordered mesostructures. Listak *et al.*[42] recently reported that polydispersity stabilized a hexagonally perforated lamellar mesostructure in poly(styrene-*b*-methyl acrylate) diblock copolymers; this structure is considered metastable in nearly monodisperse materials.[45,46] Polydispersity may also induce macrophase separation into multiple coexisting morphologies,[22,25,30] as reported in homopolymer/polydisperse diblock[10] and multicomponent diblock/diblock blends,[35–37] and as predicted for some polydisperse materials with continuous molecular weight distributions (MWDs).[30]

While AB block copolymer systems have received significant research attention, only one report (to the best of our knowledge) outside of our research program has discussed polydispersity effects in ABC triblock terpolymers. Jiang *et al.*[47] used two dimensional (2D) real space self-consistent field theory (SCFT) to study melt-phase ABC triblock terpolymers with equal interaction energies between the blocks (i.e., $\chi_{AB}=\chi_{BC}=\chi_{AC}$). Polydispersity was introduced into either the middle or terminal block using a continuous Schulz–Zimm distribution and 2D equilibrium mesostructures were identified. Although the 2D model makes comparison of structures with three dimensional systems difficult, several phenomena were described. For systems with terminal block polydispersity, domain periodicities increased monotonically with the polydispersity of the terminal block. Polydispersity in the middle block, meanwhile, promoted the formation of A/C domain interfaces.[47]

Two other relevant publications are our preliminary communications describing polydispersity-driven morphological transitions in poly(isoprene-*b*-styrene-*b*-ethylene oxide) (ISO) triblock terpolymers with equivalent volume fractions of polystyrene (PS) and polyisoprene (PI) ($f_I \approx f_S$).[48,49] Earlier studies had identified a network "window" ($0.13 < f_O < 0.24$) along this isopleth in nearly monodisperse ISO materials.[50–52] Multiply continuous network mesostructures are of interest because they can have superior mechanical properties (compared to the one dimensional and 2D counterparts)[53–55] and could be employed in, for example, catalysis,[56] photonic materials,[57] solar cell,[58,59] or separation[60] applications. Our two previous ISO polydispersity studies assessed the stability of these network mesostructures in polydisperse systems.[48,49] The first report described the phase behavior of ISO triblock terpolymers with broad, continuous MWDs in the middle PS block ($M_w/M_n = 1.31, 1.44$).[48] Two- and three-domain lamellar (LAM) phases, referred to as LAM_2 and LAM_3, were identified in the network window, indicating that the PS polydispersity drove a morphological transition away from a network mesostructure.[48] (Here we note that the distinction between LAM_2 and LAM_3, which share a common symmetry, is somewhat arbitrary.)[48] The second publication detailed a morphological transition driven by polydispersity in the terminal poly(ethylene oxide) (PEO) block.[49] In this latter work, the PEO MWD was broadened by blending several narrowly distributed ISO triblock terpolymers that were prepared from a common parent diblock (PS $M_w/M_n=1.06$). While a nearly monodisperse ISO triblock with $f_O=0.33$ adopted LAM_3, an ISO blend with the same composition and a PEO $M_w/M_n=1.30$ formed the core-shell gyroid (CSG) network.[49]

The present manuscript provides a comprehensive presentation and discussion of polydispersity effects in ISO triblock terpolymers. To interrogate the effects of polydispersity in the middle PS block, four hydroxyl-terminated poly(isoprene-*b*-styrene) (IS-OH) diblocks with comparable number-average molecular weights and volume compositions ($f_I \approx f_S$) but different PS MWDs ($M_w/M_n = 1.06, 1.16, 1.31, 1.44$) were synthesized by anionic polymerization. A total of 38 ethylene oxide polymerizations were initiated from these four IS-OH diblocks, yielding four series of ISO triblocks spanning the network window ($0.13 < f_O < 0.24$) established in the nearly monodisperse materials.[50–52] Furthermore, 13 multicomponent blends of ISO materials (PS $M_w/M_n=1.06$) were prepared at four different compositions to systematically explore the effects of varying the PEO MWD. The phase behavior of these 51 samples is characterized using small-angle X-ray scattering (SAXS) and dynamic mechanical spectroscopy (DMS). Numerous polydispersity-driven morphological transitions are reported, including transitions from LAM to CSG, from CSG to HEX, and from network morphologies [either CSG or O^{70} (the orthorhombic *Fddd* network, space group number 70)[61]] to LAM. SCFT calculations supplement the experimental

analysis and enable us to provide insight into the statistical mechanical phenomena underlying the polydispersity effects. These results support the notion that polydispersity can be employed as a tool to tune block polymer phase behavior.[62,63]

II. EXPERIMENTAL PROCEDURES

A. Polymer synthesis

All polymers were synthesized under an inert argon atmosphere using established Schlenk techniques.[64] Cyclohexane was purified by sequential passage through activated alumina followed by Q-5 (Englehard), while tetrahydrofuran was purified by passage through activated alumina.[65] Four IS-OH diblock copolymers were prepared using two different living anionic polymerization strategies; all isoprene and styrene polymerizations were allowed to proceed for at least 8 h to ensure essentially complete monomer conversion. Diblock IS(1.06)-OH (PS $M_w/M_n=1.06$) was prepared using a method designed to minimize the PI and PS block polydispersities. In this procedure, *sec*-butyllithium was used to initiate an isoprene polymerization in cyclohexane at 40 °C (~94% 1,4 addition). An aliquot (~3 ml of solution) was extracted from the reactor and terminated via precipitation in degassed methanol; the PI chains therein were analyzed using size exclusion chromatography (SEC) calibrated with PI standards to provide M_n and M_w/M_n of the PI block. Styrene was then added to the reactor and polymerized before ethylene oxide was added to end cap the IS diblock with an oxanion.[66] Degassed methanol was injected into the reactor to terminate the living chains and create terminal hydroxyl groups; the polymer was recovered by precipitation into methanol. The PI chains in the IS-OH diblock were degraded by ozonolysis (see below) and the PS block was recovered; subsequent SEC analyses using PS standards yielded M_n and M_w/M_n of this block.

Three other IS-OH diblock copolymers were prepared using a protocol designed to yield broader PS block MWDs. Three styrene polymerizations were initiated by the functional organolithium 3-triisopropylsilyloxy-1-propyllithium (TIPSOPrLi).[67] Cyclohexane and TIPSOPrLi were thermostated at 40 °C and styrene monomer was added to the reactor at different rates to vary the PS polydispersity. Living polystyryllithium chains (~3 ml of solution) were removed from the reactor, terminated via precipitation in degassed methanol, and analyzed using SEC calibrated with PS standards to determine M_n and M_w/M_n of the three PS blocks. PS M_w/M_n values of 1.31 and 1.44 are generally expected when styrene is rapidly added to a TIPSOPrLi solution over a short time interval (<2 s).[67] The PS M_w/M_n value of 1.16 is generally expected when the TIPSOPrLi is "seeded" with styrene by adding three aliquots of styrene monomer (~0.5 g) to the reactor in successive 20 min intervals before adding the balance of the styrene.[67] Isoprene was then added to the reactors and polymerized before degassed methanol was injected to terminate the living chains. The SI diblock copolymers were recovered via precipitation in methanol, dissolved in tetrahydrofuran, and reacted with tetra(*n*-butyl)ammonium fluoride to unmask the α-hydroxyl group following an established protocol.[67]

The four parent IS-OH diblocks were freeze dried from benzene before PEO chains were grown to yield ISO triblocks. Freeze dried IS-OH powder was dissolved in tetrahydrofuran stirring at 40 °C and the ethylene oxide polymerizations were initiated with potassium naphthalenide following an established protocol.[68] These reactions were allowed to proceed for at least 40 h before the living chains were terminated with degassed methanol. ISO triblocks were subsequently dissolved in dichloromethane and washed with distilled water to remove excess salts in accordance with reported procedures.[66,68] The ISO triblock terpolymers were recovered from the dichloromethane solution by precipitation in isopropanol and were then freeze dried from benzene. Multicomponent ISO blends were prepared by dissolving ISO triblocks in benzene, stirring the polymers at room temperature for at least 1 h, and freeze drying the samples from benzene.

B. Ozonolysis

The IS(1.06)-OH diblock (~0.5 g) was dissolved in toluene (~30 ml) and the solution was cooled to −78 °C using a dry ice bath. Ozone was generated using an OREC Ozone Systems V Series instrument operating with 1.5 A of current and the gas was bubbled through the stirring toluene solution at a rate of 1 ml/min for 5 min to degrade the PI. The PS block was recovered by precipitation in methanol and analyzed; ^{1}H NMR analysis confirmed that PI degradation was complete and SEC analysis provided M_w/M_n for the PS block.

C. Molecular characterization

The compositions of the neat ISO triblock terpolymers and the ISO blends were determined using a 300 MHz Varian NMR spectrometer. The instrument was operated at room temperature and deuterated chloroform was employed as the solvent. Block mole fractions were computed using the integrated ^{1}H NMR spectra and converted to volume fractions f_I, f_S, and f_O using published homopolymer densities at 140 °C ($\rho_I=0.830$, $\rho_S=0.969$, $\rho_O=1.064$ g/cm^3).[69]

SEC experiments were performed at 30 °C on a Waters 717 GPC equipped with three Polymer Labs Mixed-C columns and a Waters 410 differential refractometer. Tetrahydrofuran was used as the mobile phase, with a flow rate of 1.0 ml/min. Calibration curves were constructed using either six PI standard samples ($1000<M_n<27000$ g/mol, Scientific Polymer Products) or ten PS standard samples ($580<M_n<377400$ g/mol, Polymer Labs). The PI calibration was used to measure M_n and M_w/M_n of the PI aliquot, while the PS calibration was employed to determine M_n and M_w/M_n of the PS aliquots and M_w/M_n of all other polymers. M_n values of the IS-OH diblocks were computed using the M_n's of the initiated PI (PS) blocks and the masses of styrene (isoprene) subsequently added to the reactor. The actual compositions were verified by ^{1}H NMR spectroscopy which indicated that essentially complete additions of isoprene and

styrene monomers had been achieved. ISO M_n values were calculated from M_n's of the IS diblocks and the overall compositions measured using ^{1}H NMR spectroscopy. SEC analyses indicated that less than 5% of terminated PI or PS homopolymers and IS diblocks were present in the ISO triblock samples.

D. Synchrotron SAXS

Synchrotron SAXS experiments were conducted at the Advanced Photon Source at Argonne National Laboratory using the equipment maintained by the DuPont-Northwestern-Dow Collaborative Access Team (DND-CAT). Two different sample-to-detector distances (providing equivalent data for our purposes) were employed with an X-ray wavelength (λ) of 0.8856 Å: (1) 5.47 m and (2) 8.56 m. Distances in both cases were calibrated using silver behenate. Polymer powders were packed inside o-rings ($\approx$2 mm thick) and sealed inside differential scanning calorimeter (DSC) pans. Sample temperatures were controlled with a liquid nitrogen-cooled DSC chamber operating under a helium purge. Specimen heating and cooling rates were rapid ($\approx$50 °C/min), and all samples were heated 10 °C above T_{ODT} (when possible) or to 250 °C for 5 min before data were collected in an effort to erase effects due to thermal history. Extensive experience with DSC experiments shows that a 5 min thermal soak is sufficient to achieve thermal equilibrium in these small specimens. Samples were held at target temperatures for 5 min before data were collected on a Mar charge coupled device area detector. The 2D diffraction intensities measured by the detector were azimuthally averaged and the data are presented in this manuscript as plots of intensity (I) on an arbitrary scale versus the scattering wave-vector modulus [$q=|\mathbf{q}|=4\pi/\lambda \sin(\theta/2)$, where θ is the scattering angle].

E. Dynamic mechanical spectroscopy

DMS experiments were conducted on a Rheometrics Scientific ARES strain-controlled rheometer equipped with 25 mm diameter parallel plates. All experiments were performed in an inert nitrogen atmosphere. Polymer powders were placed on the parallel plates, melted at 100 °C, and annealed 10 °C above T_{ODT} (when possible) or at 250 °C for 10 min in an effort to erase effects due to thermal history. Isochronal ($\omega=1$ rad/s) dynamic elastic (G') and loss (G'') moduli measurements were obtained while heating and cooling the samples at 1–2 °C/min. All data were acquired using a low strain amplitude (1%–2%) that was determined to be within the linear viscoelastic regime.

III. EXPERIMENTAL RESULTS AND ANALYSIS

A total of 38 ISO triblock terpolymers with nearly equivalent volume fractions of PS and PI ($f_I \approx f_S$) were synthesized from four separate parent IS-OH diblock copolymers. The parent diblocks have narrow MWDs in the PI blocks but different PS polydispersities. These polymers are labeled using the notation IS(PDI$_S$)O(f_O), where PDI$_S$ is the PDI of the PS block and f_O is the volume fraction of the PEO. The molecular characterization data for all of the neat ISO triblock terpolymers are presented in Table I and summarized in Fig. 1, with the data for some of the polymers being reproduced from our preliminary publications.[48,49] A series of previously characterized[50–52] higher molecular weight ISO samples is also included in Table I. These samples are labeled using the original ISOi notation of Bailey *et al.*[50] and the characterization data are reproduced from the report of Epps *et al.*[52]

The morphology assignments and lattice dimensions were determined using SAXS data. Order-disorder transition temperatures (T_{ODT}'s) were measured using DMS; T_{ODT} is associated with the temperature at which the dynamic elastic modulus (G') discontinuously decreases while heating a sample.[70] In all cases the T_{ODT} determined from DMS was consistent with the SAXS data. T_{ODT}'s above 250 °C were not accessed because thermal degradation of the materials may occur at these elevated temperatures. We have identified order-order phase transitions (OOTs) from CSG to PEO cylinders packed hexagonally in an IS matrix (HEX$_O$) in samples IS(1.06)O(0.13) and IS(1.06)O(0.20) and from LAM$_3$ to O^{70} in triblock IS(1.16)O(0.25). Morphological coexistence is reported in samples IS(1.06)O(0.28) and IS(1.44)O(0.24), as Bragg peaks consistent with CSG and O^{70} are present in the SAXS data obtained from these polymers. For these materials, the morphology with the higher peak intensities is listed on the left in Table I and the reported lattice parameters correspond to this mesostructure. While it is possible coexistence represents the equilibrium states of these specimens,[30] an accurate assessment of thermodynamic stability would require lengthy annealing times at a synchrotron facility and is beyond the scope of this manuscript.

Thirteen blends of nominally monodisperse ISO triblock terpolymers were prepared at four different compositions. Eleven of the blends contain ISO samples prepared from IS(1.06)-OH; the other two blends are comprised of higher molecular weight ISO materials synthesized by Bailey *et al.*[50] The blends are labeled using the notation ISO(PDI$_O$,f_O), where f_O is the overall PEO volume fraction in the blend and PDI$_O$ is the PDI of the PEO block calculated by assuming that all of the neat triblocks have perfectly monodisperse PEO chains. The characterization data obtained for these blends are listed in Table II and summarized in Fig. 1, and the mass fractions of the ISO triblocks in each blend are provided in Table SI of the Supporting Information.[71]

A. IS(1.06)O triblock terpolymers

Twelve IS(1.06)O triblocks were synthesized from the parent IS(1.06)-OH diblock material. The morphologies of all IS(1.06)O samples were identified using SAXS. In all cases, the SAXS data were consistent with the DMS analyses. Representative synchrotron SAXS powder patterns for IS(1.06)O(0.05), IS(1.06)O(0.26), IS(1.06)O(0.27), and IS(1.06)O(0.33) are provided in Fig. 2; the patterns for IS(1.06)O(0.05) and IS(1.06)O(0.33) are reproduced from our preliminary publication.[49] The SAXS data for IS(1.06)O(0.26), IS(1.06)O(0.27), and IS(1.06)O(0.33) were

TABLE I. Neat ISO characterization data.

Polymer	N_I[a]	N_S[a]	N_O[a]	f_O[b]	M_n (kDa)	M_w/M_n	Lattice dimensions (nm)[c]	Phase[d]	T_{ODT}[e] (°C)
IS(1.06)–OH[f]	81	84	0	0	10.6	1.08	12.5 (80 °C)	DIS	
IS(1.06)O(0.05)[f]	81	84	9	0.05	11.3	1.10	13.9 (80 °C)	LAM_2	88
IS(1.06)O(0.10)[f]	81	84	19	0.10	12.0	1.13	37.0	CSG	127
IS(1.06)O(0.13)[f]	81	84	25	0.13	12.5	1.13	38.6	CSG→HEX_O[g]	155
IS(1.06)O(0.20)[f]	81	84	41	0.20	13.7	1.11	42.3	CSG→HEX_O[g]	230
IS(1.06)O(0.21)[f]	81	84	44	0.21	13.9	1.10	44.0	CSG	242
IS(1.06)O(0.23)[f]	81	84	49	0.23	14.3	1.14	45.1	CSG	>250
IS(1.06)O(0.26)[f]	81	84	58	0.26	15.0	1.11	46.3	CSG	>250
IS(1.06)O(0.27)[f]	81	84	61	0.27	15.2	1.13	0.280, 0.577, 76.9	O^{70}	>250
IS(1.06)O(0.28)[f]	81	84	64	0.28	15.4	1.12	0.280, 0.578, 77.3	O^{70}/CSG[h]	>250
IS(1.06)O(0.33)[f]	81	84	81	0.33	16.7	1.14	20.2	LAM_3	>250
IS(1.06)O(0.35)[f]	81	84	89	0.35	17.3	1.16	20.7	LAM_3	>250
IS(1.06)O(0.44)[f]	81	84	130	0.44	20.4	1.19	23.0	LAM_3	>250
IS(1.16)–OH	80	84	0	0	10.5	1.12	12.6 (80 °C)	DIS	
IS(1.16)O(0.11)	80	84	20	0.11	12.0	1.14	0.294, 0.584, 62.9	O^{70}	139
IS(1.16)O(0.13)	80	84	25	0.13	12.4	1.10	0.294, 0.578, 64.2	O^{70i}	160
IS(1.16)O(0.15)	80	84	29	0.15	12.7	1.11	0.295, 0.578, 65.9	O^{70i}	174
IS(1.16)O(0.20)	80	84	41	0.20	13.6	1.11	0.292, 0.578, 69.1	O^{70}	221
IS(1.16)O(0.21)	80	84	44	0.21	13.8	1.12	0.292, 0.578, 72.3	O^{70}	229
IS(1.16)O(0.25)	80	84	55	0.25	14.7	1.14	19.4	LAM_3→O^{70j}	>250
IS(1.16)O(0.31)	80	84	75	0.31	16.2	1.13	20.4	LAM_3	>250
IS(1.16)O(0.34)	80	84	85	0.34	16.9	1.15	20.9	LAM_3	>250
IS(1.31)–OH	88	91	0	0	11.5	1.17	13.6 (80 °C)	DIS	
IS(1.31)O(0.04)	88	91	7	0.04	12.1	1.20	14.7 (90 °C)	LAM	93
IS(1.31)O(0.09)	88	91	18	0.09	12.8	1.21	15.8 (100 °C)	LAM	112
IS(1.31)O(0.11)	88	91	22	0.11	13.2	1.16	15.9	LAM	140
IS(1.31)O(0.14)	88	91	29	0.14	13.7	1.13	16.5	LAM	147
IS(1.31)O(0.17)	88	91	37	0.17	14.3	1.18	17.1	LAM	157
IS(1.31)O(0.24)	88	91	57	0.24	15.8	1.15	18.0	LAM	190
IS(1.31)O(0.30)	88	91	77	0.30	17.3	1.11	19.0	LAM	195
IS(1.44)–OH	86	89	0	0	11.2	1.15	13.5 (80 °C)	LAM	
IS(1.44)O(0.04)	86	89	7	0.04	11.8	1.13	14.8 (100 °C)	LAM	103
IS(1.44)O(0.05)	86	89	9	0.05	11.9	1.16	15.1 (100 °C)	LAM	121
IS(1.44)O(0.09)	86	89	17	0.09	12.5	1.14	15.4	LAM	146
IS(1.44)O(0.10)	86	89	19	0.10	12.7	1.13	15.9	LAM	151
IS(1.44)O(0.12)	86	89	24	0.12	13.0	1.14	16.2	LAM	165
IS(1.44)O(0.14)	86	89	29	0.14	13.4	1.14	16.7	LAM	180
IS(1.44)O(0.16)	86	89	33	0.16	13.7	1.13	16.9	LAM	184
IS(1.44)O(0.17)	86	89	36	0.17	13.9	1.13	0.290, 0.578, 69.5	O^{70}	201
IS(1.44)O(0.21)	86	89	47	0.21	14.7	1.11	18.0	LAM[k]	216
IS(1.44)O(0.22)	86	89	50	0.22	15.0	1.12	0.291, 0.578, 72.8	O^{70}	>250
IS(1.44)O(0.24)	86	89	55	0.24	15.4	1.15	48.6	CSG/O^{70l}	>250
IS–OH3[m]	106	106	0	0	13.6	1.05	15.8 (85 °C)	LAM_2	97
ISO1[m]	106	106	3	0.02	13.8	1.05	16.1 (105 °C)	LAM_2	111
ISO5[m]	106	106	10	0.05	14.3	1.05	16.4 (100 °C)	LAM_2	134
ISO2[m]	106	106	14	0.06	14.6	1.06	16.9 (110 °C)	LAM_2	146
ISO10[m]	106	106	77	0.27	19.4	1.06	23.0 (160 °C)	LAM_3	>250
ISO11[m]	106	106	90	0.30	20.4	1.05	24.1 (160 °C)	LAM_3	>250
ISO12[m]	106	106	109	0.34	21.8	1.06	25.3 (160 °C)	LAM_3	>250

[a]Number-average degrees of polymerization (N_i) based on a segment reference volume of 118 $Å^3$ and calculated using published density values at 140 °C (ρ_I=0.830, ρ_S=0.969, ρ_O=1.064 g/cm^3) (Ref. 69).
[b]Volume fractions calculated from the provided N values.
[c]Lattice dimensions are obtained from SAXS data and are reported at 120 °C unless otherwise noted in parentheses (°C). The lattice dimensions listed for O^{70} correspond to a/c, b/c, and c and the values listed for disordered samples correspond to the length scales associated with the principal scattering vectors.
[d]Morphologies identified using SAXS data.
[e]Measured using DMS.
[f]M_w/M_n value for the PI block measured using SEC is 1.10.
[g]Samples IS(1.06)O(0.13) and IS(1.06)O(0.20) undergo OOTs from CSG to HEX_O at 148 and 217 °C, respectively.
[h]Bragg peaks characteristic of both O^{70} and CSG are identified at 120 °C; the intensities of the O^{70} peaks are higher and the listed lattice parameters are for O^{70}.
[i]Some low intensity peaks in these SAXS data are not consistent with O^{70}, suggesting a small fraction of these materials (<5%) forms a different, undetermined mesostructure.
[j]Specimen IS(1.16)O(0.25) undergoes an OOT from LAM_3 to O^{70} at 160 °C.
[k]A transient O^{70} mesostructure was identified above 185 °C (Ref. 48).
[l]One small Bragg peak in the SAXS data obtained at 120 °C is inconsistent with CSG; the remaining peaks are indexed to CSG and the listed domain periodicity is for CSG. The location of the non-CSG peak is, assuming the principal peak corresponds to the 111 position, consistent with the 113 reflection from the O^{70} mesostructure.
[m]Polymers were previously characterized (Refs. 50–52) and are labeled using the notation of Bailey *et al.* (Ref. 50).

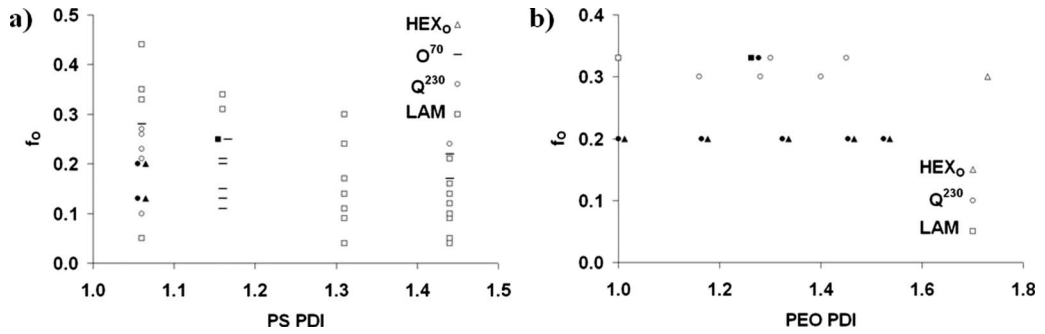

FIG. 1. Plots summarizing the morphologies identified in ISO triblock terpolymers as a function of composition and either the (a) PS or (b) PEO PDI. All of the materials have comparable PI and PS molecular weights and have compositions that lie on the $f_I \approx f_S$ isopleth (see Tables I and II). The pairs of adjacent solid symbols indicate an OOT upon heating. Here we note that a distinction between LAM_2 and LAM_3, which share a common symmetry, is somewhat arbitrary based on SAXS data alone and thus not made in Fig. 1 (Ref. 48). We expect that LAM_3 is the likely morphology at higher PEO contents.

acquired at 120 °C, while the data for IS(1.06)O(0.05) were collected at 80 °C. The Bragg patterns for IS(1.06)O(0.05) and IS(1.06)O(0.33) are indexed to lamellae; the absence of the 002 peak in the IS(1.06)O(0.05) data is consistent with a structure factor extinction for symmetric LAM_2.[52] The rich assortments of peaks in the IS(1.06)O(0.26) and IS(1.06)O(0.27) data are indexed to CSG and O^{70}, respectively. The allowed reflections for the orthorhombic lattice of O^{70} are not simple multiples of the primary peak q^*, as they are for a cubic lattice such as CSG. Rather, the orthorhombic peak positions change with the lattice dimensions a, b, and c according to $q_{hkl}=2\pi[h^2/a^2+k^2/b^2+l^2/c^2]^{1/2}$, where h, k, and l are the associated Miller indices. Specific orthorhombic space groups are associated with different sets of allowed reflections, as identified in the crystallographic tables.[61] The a, b, and c lattice parameters were varied to obtain the optimal least-squares fit of the allowed reflections for O^{70} to the recorded SAXS peaks; an example of this indexing scheme is provided in Fig. 2(c) for specimen IS (1.06)O(0.27) .

Four multicomponent blends of IS(1.06)O triblocks were prepared with an overall $f_O=0.20$. Isochronal ($\omega=1$ rad/s) G' measurements were employed to interrogate the viscoelastic response of these materials; all samples were annealed 10 °C above T_{ODT} (or at 250 °C) for 10 min prior to data collection in an effort to erase effects associated with thermal history. G' discontinuously decreased upon heating (and increased during cooling) for all of these blends [and neat triblocks IS(1.06)O(0.13) and IS(1.06)O(0.20), see Fig. S1 in Supporting Information[71]] This sharp change in G' is consistent with an OOT, and T_{OOT} is assigned to the onset temperature at which G' discontinuously changes upon heating. While heating/cooling hysteresis was present in all G' traces, the eventual recovery of G' on cooling suggests that the OOT is reversible. SAXS experiments were utilized to probe the mesostructures of these materials as a function of temperature. Representative SAXS data obtained for blend ISO(1.46, 0.20) at 120 and 250 °C are provided in Fig. 3. The Bragg peaks obtained at 120 °C are indexed to CSG and those acquired at 250 °C are indexed to a hexagonal morphology. Assuming this hexagonal mesostructure is hexago-

TABLE II. ISO blend characterization data.

Blend	N[a]	M_n (kDa)	f_O[a]	PDI$_O$[b]	Lattice dimensions (nm)[c]	Phase[d]	T_{OOT}[e] (°C)	T_{ODT} (°C)
ISO(1.17, 0.20)	206	13.7	0.20	1.17	43.6	CSG→HEX$_O$	195	>250
ISO(1.33, 0.20)	206	13.7	0.20	1.33	44.1	CSG→HEX$_O$	165	>250
ISO(1.46, 0.20)	206	13.7	0.20	1.46	44.3	CSG→HEX$_O$	150	>250
ISO(1.53, 0.20)	206	13.7	0.20	1.53	44.8	CSG→HEX$_O$	142	>250
ISO(1.16, 0.30)	236	16.0	0.30	1.16	50.5	CSG	···	>250
ISO(1.28, 0.30)	236	16.0	0.30	1.28	51.4	CSG	···	>250
ISO(1.40, 0.30)	236	16.0	0.30	1.40	52.4	CSG	···	>250
ISO(1.73, 0.30)	236	16.0	0.30	1.73	22.9	HEX$_O$	···	>250
ISO(1.27, 0.33)	246	16.7	0.33	1.27	53.6[f]	LAM$_3$→CSG	210	>250
ISO(1.30, 0.33)	246	16.7	0.33	1.30	53.6	CSG	···	>250
ISO(1.45, 0.33)	246	16.7	0.33	1.45	55.5	CSG	···	>250
ISO(1.17, 0.27)	289	19.4	0.27	1.17	55.1 (160 °C)	CSG	···	>250
ISO(1.30, 0.27)	289	19.4	0.27	1.30	56.8 (160 °C)	CSG	···	>250

[a]Number-average values based on a segment reference volume of 118 Å^3 (for N_i) and calculated using published density values at 140 °C ($\rho_I=0.830$, $\rho_S=0.969$, $\rho_O=1.064$ g/cm^3) (Ref. 69).
[b]Calculated for the PEO block by assuming that the PEO chains in the component ISO triblocks are perfectly monodisperse.
[c]Lattice dimensions are obtained from SAXS data and are reported at 120 °C unless otherwise noted in parentheses (°C).
[d]Morphologies identified using SAXS data. When two morphologies are listed, the one on the left is the low temperature structure and the one on the right is the high temperature phase.
[e]Measured using DMS; the T_{OOT} listed is the temperature at which the slope in G' sharply changes upon heating.
[f]Domain periodicity of the long-lived metastable CSG at 120 °C.

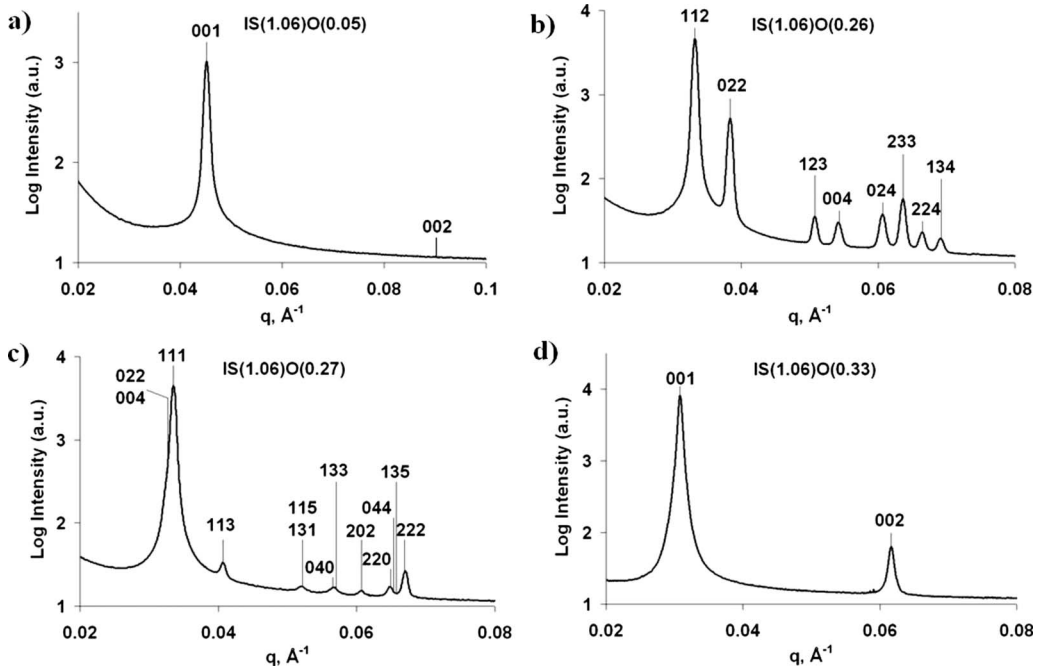

FIG. 2. Synchrotron SAXS data acquired at 120 °C [80 °C for IS(1.06)O(0.05)]. All samples were annealed at 250 °C for 5 min [at 100 °C for IS(1.06)O(0.05)] before data were collected. The data for (a) IS(1.06)O(0.05) and (d) IS(1.06)O(0.33) are indexed to a lamellar morphology; the absence of the 002 peak in the IS(1.06)O(0.05) data is consistent with a structure factor extinction for symmetric LAM_2 (Ref. 52). The Bragg peaks for (b) IS(1.06)O(0.26) are indexed to CSG and the diffraction pattern for (c) IS(1.06)O(0.27) is indexed to O[70].

nally packed cylinders, two configurations are possible: PEO cylinders packed hexagonally in an IS matrix (HEX_O) and PI cylinders packed hexagonally in a SO matrix (HEX_I).[72] As will be discussed in Sec. IV, HEX_O has a lower calculated free energy than HEX_I for all of the samples in this study. This result leads us to identify the hexagonal morphology as HEX_O. Similar SAXS data were obtained for the other blends with f_O=0.20 and for the neat triblocks IS(1.06)O(0.13) and IS(1.06)O(0.20); all of these samples undergo an OOT from CSG to HEX_O upon heating.

Four IS(1.06)O blends were prepared with an overall f_O=0.30. There were no discontinuities in the isochronal G' measurements (data not shown) for any of these samples, suggesting none of the materials undergo OOTs between 100 and 250 °C. SAXS data were consistent with these DMS measurements, as the relative peak positions varied only slightly with temperature for each blend. SAXS data acquired at 120 °C for samples ISO(1.40, 0.30) and ISO(1.73, 0.30) are presented in Fig. 4. The Bragg pattern for ISO(1.40, 0.30) is indexed to CSG; similar data were acquired for samples ISO(1.16, 0.30) and ISO(1.28, 0.30). The peaks for specimen ISO(1.73, 0.30) are indexed to a hexagonal morphology (HEX_O).

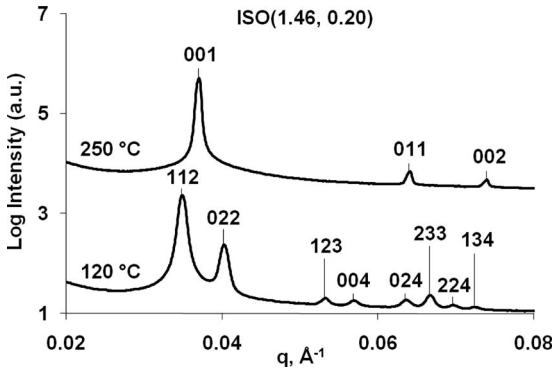

FIG. 3. SAXS data acquired at 120 and 250 °C for ISO(1.46, 0.20). The sample was annealed for 5 min at each target temperature prior to data collection (250 °C anneal preceded 120 °C anneal). The Bragg pattern at 120 °C is indexed to CSG while the peaks at 250 °C are indexed to a hexagonal mesostructure (here identified as HEX_O).

Three IS(1.06)O blends were prepared with an overall f_O=0.33. There are no discontinuities in the G' data acquired for blends ISO(1.30, 0.33) and ISO(1.45, 0.33), suggesting these samples do not undergo OOTs. SAXS data (not shown) are consistent with this DMS analysis and are used to identify the mesostructure of these samples as CSG over temperatures ranging from 100 to 250 °C. The isochronal G' data for blend ISO(1.27, 0.33) increase sharply at 210 °C upon heating, consistent with an OOT; recovery of G' during cooling suggests the transition is reversible. SAXS data obtained at 120 and 250 °C for sample ISO(1.27, 0.33) are presented in Fig. 5. The material was heated to 120 °C and then to 250 °C, with 4 min anneals prior to data collection at each temperature. The Bragg pattern acquired at 120 °C is indexed to LAM_3, while the 250 °C peaks are indexed to CSG; these morphology assignments are consistent with the G' measurements. The blend was subsequently cooled (at ~50 °C/min) to 120 °C and annealed for 4 min. Interestingly, the SAXS data collected at 120 °C upon cooling did not index to LAM_3, but were consistent with CSG. Since an OOT was evident (by a discontinuous decrease in G') in the DMS measurements with a slower 1 °C/min cooling rate, the CSG present at 120 °C upon cooling in the SAXS experiment is likely a long-lived metastable mesostructure.

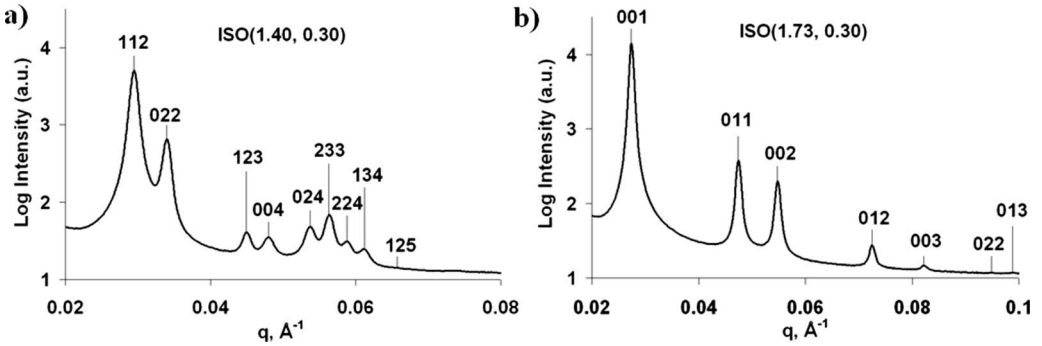

FIG. 4. Synchrotron SAXS data acquired at 120 °C for two IS(1.06)O blends with overall f_O=0.30. The polymers were annealed at 250 °C for 5 min prior to a 5 min anneal and data collection at 120 °C. (a) ISO(1.40, 0.30) SAXS data are indexed to CSG and (b) ISO(1.73, 0.30) Bragg peaks are indexed to a hexagonal morphology (here identified as HEX_O).

This result is consistent with reports of gyroid persisting as a long-lived metastable morphology in several AB diblock copolymer systems.[45,73]

Two ISO blends with an overall f_O=0.27 were prepared using the ~15% higher molecular weight ISO triblock terpolymers that were previously synthesized and characterized by Bailey *et al.* (see Table I).[50–52] The neat ISO10 triblock (f_O=0.27) forms LAM_3 at temperatures ranging from 100 to 250 °C. SAXS and DMS data (not shown) indicate that the ISO(1.17, 0.27) and ISO(1.30, 0.27) blends with the same overall M_n and composition as ISO10 adopt a CSG mesostructure over an identical temperature range. These results demonstrate that polydispersity can be employed to drive morphological transitions at higher molecular weights and is not limited as a tool to the molecular weights of the IS(1.06)O series of polymers.

B. IS(1.16)O triblock terpolymers

Eight IS(1.16)O triblocks were synthesized from the IS(1.16)-OH parent diblock. SAXS patterns (not shown) that are indexed to O^{70} were acquired at all temperatures below T_{ODT} for samples IS(1.16)O(0.11), IS(1.16)O(0.20), and IS(1.16)O(0.21). The SAXS data obtained for samples IS(1.16)O(0.13) and IS(1.16)O(0.15) contain a few low intensity peaks that are not consistent with O^{70} (see Fig. S2 in the Supporting Information[71]). The low intensities of these extra peaks make identification of potential coexisting morphologies difficult. However, since the peaks consistent with O^{70} dominate these Bragg patterns, that network mesostructure is assigned as the morphology in Table I. SAXS data (not shown) consistent with LAM_3 were acquired at temperatures ranging from 100 to 250 °C for specimens IS(1.16)O(0.31) and IS(1.16)O(0.34). Only specimen IS(1.16)O(0.25) undergoes an OOT. The G' data obtained while heating this sample exhibit a sharp increase at 160 °C; recovery of G' during cooling suggests the transition is reversible. Synchrotron SAXS data collected above and below 160 °C are provided in Fig. 6. The Bragg peaks at 120 °C are indexed to LAM_3 and those at 200 °C are indexed to O^{70}; these data confirm the material undergoes an OOT from LAM_3 to O^{70} at 160 °C. There is a low intensity peak in the 120 °C data (marked with ♦) that is consistent with the 113 reflection for O^{70}; a small portion of the material is likely (given the short 5 min annealing time) trapped in a metastable O^{70} configuration.

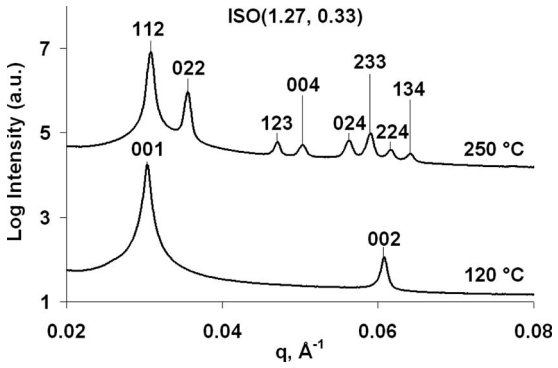

FIG. 5. SAXS data acquired at 120 and 250 °C for blend ISO(1.27, 0.33). The sample was annealed for 4 min at each target temperature prior to data collection (120 °C anneal preceded 250 °C anneal). The Bragg pattern at 120 °C is indexed to LAM_3, while the peaks at 250 °C are indexed to CSG.

C. IS(1.31)O triblock terpolymers

Seven IS(1.31)O triblocks were prepared from the IS(1.31)-OH parent diblock; characterization of these samples was reported in an earlier communication.[48] None of these materials have discontinuous changes in G' that are

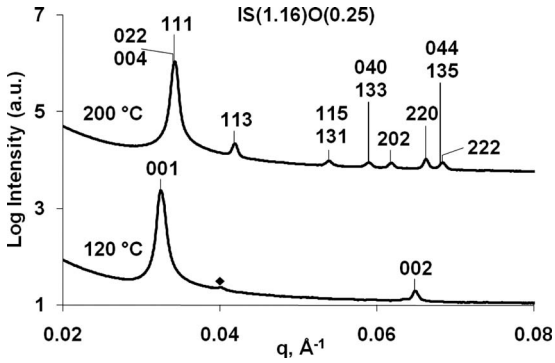

FIG. 6. SAXS data acquired at 120 and 200 °C for sample IS(1.16)O(0.25). The sample was annealed for 5 min at 250 °C and then annealed for 5 min at each target temperature prior to data collection (200 °C anneal preceded 120 °C anneal). The Bragg pattern at 120 °C is indexed to LAM_3 while the peaks at 200 °C are indexed to O^{70}. The low intensity peak in the 120 °C data (marked with ♦) corresponds to the 113 reflection from O^{70} and is consistent with a small fraction of the material being trapped in a metastable O^{70} mesostructure.

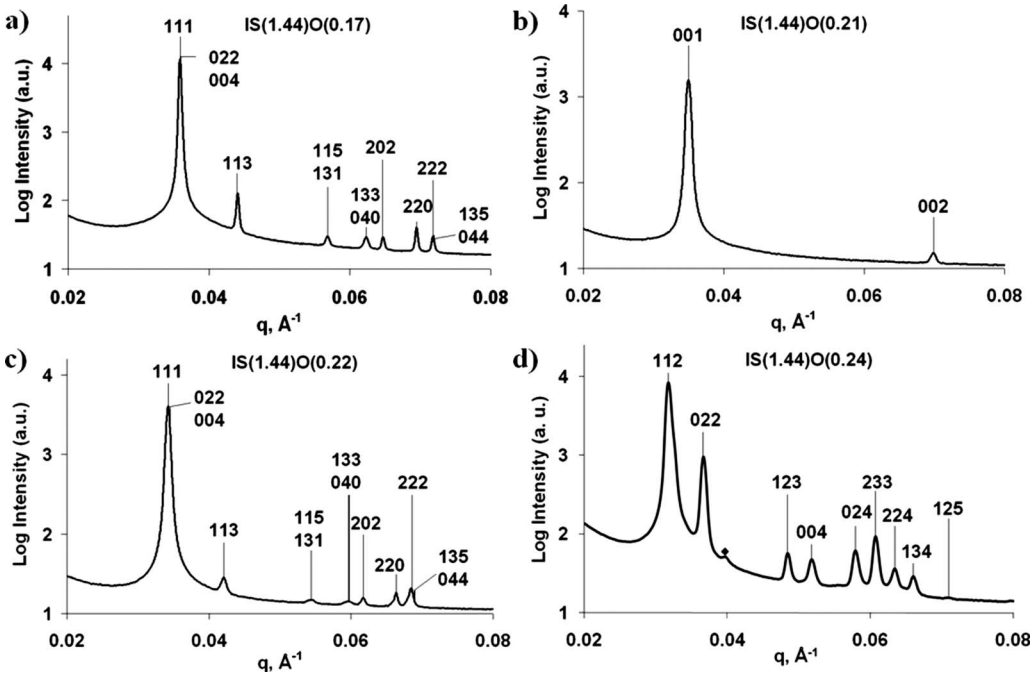

FIG. 7. SAXS data acquired at 120 °C for samples (a) IS(1.44)O(0.17), (b) IS(1.44)O(0.21), (c) IS(1.44)O(0.22), and (d) IS(1.44)O(0.24). All of the materials were annealed at 250 °C for 5 min before they were held at 120 °C for 5 min. The peaks for (a) IS(1.44)O(0.17) and (c) IS(1.44)O(0.22) are indexed to O^{70}, those for (b) IS(1.44)O(0.21) are indexed to LAM, and those for (d) IS(1.44)O(0.24) are indexed to CSG. The low intensity peak in the IS(1.44)O(0.24) data (marked with a ♦) is consistent with the 113 reflection for O^{70}; a small portion of the material has formed O^{70} that coexists with the CSG network.

characteristic of OOTs and SAXS data for all of these samples index to a lamellar morphology, termed LAM. LAM_2 and LAM_3 are not differentiated in this series of IS(1.31)O triblocks because no other mesostructure was identified along the $f_I \approx f_S$ isopleth. The lack of an intermediate morphology suggests the composition profiles continuously vary as f_O increases and renders arbitrary a morphological assignment of LAM_2 or LAM_3.

D. IS(1.44)O triblock terpolymers

Eleven IS(1.44)O triblocks were synthesized from the IS(1.44)-OH parent diblock. The characterization data obtained from eight of these polymers [those with $f_O \leq 0.16$ and triblock IS(1.44)O(0.21)] were reported in our preliminary publication[48] In that communication, SAXS data were used to identify LAM in all eight samples, although a transient O^{70} morphology was identified above 185 °C in specimen IS(1.44)O(0.21) (see Fig. S3 in the Supporting Information[71] for details).[48] This transient O^{70} structure always transitioned to LAM during thermal annealing at temperatures above 185 °C (<15 min anneals). Triblocks IS(1.44)O(0.17), IS(1.44)O(0.22), and IS(1.44)O(0.24) were prepared to probe the stability of the O^{70} network at compositions close to that of sample IS(1.44)O(0.21). SAXS data acquired at 120 °C for these four samples are provided in Fig. 7. The Bragg peaks for IS(1.44)O(0.17) and IS(1.44)O(0.22) are indexed to O^{70}, the data for IS(1.44)O(0.21) are indexed to LAM, and the powder pattern for IS(1.44)O(0.24) is indexed to CSG. These results clearly indicate that PS polydispersity does not always prevent the formation of network morphologies. The SAXS pattern for specimen IS(1.44)O(0.24) contains a low intensity peak that does not index to CSG. This peak is marked with a ♦ in Fig. 7 and, assuming the principal peak corresponds to the 111 position, its location is consistent with the 113 reflection from the O^{70} mesostructure (this peak is not present in SAXS data acquired at 250 or 200 °C). The IS(1.44)O(0.24) material was subsequently annealed for 3 min at 250 °C and then for 2 h at 120 °C to probe the relative stability of the CSG and putative O^{70} morphologies. Peaks consistent with both mesostructures were still present in the SAXS data following this thermal treatment, with the O^{70} peaks growing in relative intensity (i.e., the O^{70} peaks are more prominent than they are in the data provided in Fig. 7). It is possible that coexistence of the CSG and O^{70} networks is the equilibrium state for sample IS(1.44)O(0.24) at 120 °C,[30] although more extended annealing times would be required to determine if CSG is a long-lived metastable morphology or part of the equilibrium configuration.

IV. SCFT RESULTS AND ANALYSIS

A. SCFT methodology

Comprehensive details of SCFT are available in a recently published review[74] and book;[75] only a brief synopsis of the theory is provided here. SCFT represents the molecular interactions experienced by a segment of a polymer chain as a chemical potential field. An initial chemical potential field is guessed and the modified diffusion equation for a single chain placed in this field is solved to yield a segment density profile. A new chemical potential field is then calculated from the density profile solution and the process begins anew with this new potential field; the procedure continues until the calculated potential fields and densities are self-consistent.[74,76] The same general framework applies to

multicomponent systems, although the procedural details of computing overall segment density profiles and chemical potential fields are somewhat different. In a multicomponent system, a single potential field interacts with all of the chains and the modified diffusion equation is independently solved for each chain in this field. The overall segment density profile is generated by summing the individual chain segment density profiles (weighted by their respective number fractions). The chemical potential field used in subsequent iterations is computed from this overall segment density profile.

Our SCFT calculations were performed using the code developed by Tyler *et al.*[72,77] This approach involves calculating the free energies of selected mesostructural candidates; the morphology with the lowest free energy is considered the equilibrium structure. In the implementation of Tyler *et al.*, the modified diffusion equation is solved using a pseudospectral method and the symmetry-adapted basis functions. The free energy of each candidate is then minimized with respect to the unit cell parameters using the variable-unit-cell algorithm described by Tyler and Morse.[78] Additional details of this SCFT methodology are described in the literature.[72,79]

In the current report, we do not attempt to consider all possible space group symmetries for every sample but are striving to understand the statistical mechanical phenomena underlying the phase behavior of the experimental materials described earlier. Given the experimental data described above, we selected five possible ordered morphologies: LAM, O^{70}, CSG, PEO cylinders packed hexagonally in an IS matrix (HEX_O), and PI cylinders packed hexagonally in a SO matrix (HEX_I). SAXS data consistent with LAM, O^{70}, CSG, and a phase with hexagonal symmetry were reported above for samples in this study. Here we assume the hexagonal mesostructure contains hexagonally packed cylinders; HEX_O and HEX_I are the two possible configurations of hexagonally packed cylinders in the ISO system.[72] The monomer reference volume for these calculations is 118 $Å^3$ and Flory–Huggins interaction parameters (χ), statistical segment lengths (b), and degrees of polymerization (N) are all scaled to this quantity. The χ (here taken at 100 °C)[80] and b (Refs. 69 and 81) values are adapted from the literature: $\chi_{IS}=0.044$, $\chi_{SO}=0.057$, $\chi_{IO}=0.183$, $b_I=6.07$, $b_S=5.47$, and $b_O=7.80$. These values were previously used by Tyler *et al.*[72,77]

SCFT calculations were performed on hypothetical sets of ISO triblocks that mimic those prepared experimentally. N of each IS diblock is kept constant at our experimental values and the lengths of the PEO chains are varied. The PI and PEO block length distributions are approximated as perfectly monodisperse, while the PS chain distributions are either (i) approximated as perfectly monodisperse (calculations for ISO blends) or (ii) approximated using 12–14 different PS chain lengths (calculations for materials with polydisperse PS blocks). Including significantly more than 12–14 chain lengths is not feasible because of the large amount of computational memory required for the SCFT calculations (the required memory increases roughly linearly with the number of chains). The PS chain lengths are input into the SCFT calculations in relative quantities that match their values measured experimentally using SEC (i.e., all input values lie on the SEC trace, as illustrated in Fig. S4 in the Supporting Information[71]) and the individual PS chains were selected to make the PDI and number-average N values of the input PS distributions equal those measured experimentally (within 0.01 and 0.5, respectively). (Here we note that the response of the refractive index detector in our SEC experiments is directly proportional to the mass concentration of the eluting sample.) This chain discretization strategy captures both the shape and PDI of the experimentally measured distributions; the PDI alone is not sufficient to describe polydispersity effects in block copolymers.[31]

B. IS(1.06)O free energy calculations

A plot presenting the computed free energy curves of the LAM, CSG, O^{70}, HEX_O, and HEX_I morphologies for perfectly monodisperse ISO triblocks ($N_I=81$, $N_S=84$, $0.10<f_O<0.40$) was provided in an earlier publication.[49] The molecular weights of this theoretical series match those of the IS(1.06)O triblocks and the predicted sequence of morphologies is LAM→O^{70}→LAM. This LAM→O^{70}→LAM sequence was previously reported experimentally[50–52] and theoretically[72,77] in higher segregation strength ISO materials, although there were quantitative discrepancies in the locations of the phase boundaries between experiment and theory. As discussed earlier, the experimentally measured sequence of morphologies in the IS(1.06)O series is LAM→CSG→O^{70}→LAM, not the LAM→O^{70}→LAM predicted using SCFT. The calculated free energy differences between CSG, LAM, and O^{70} are, however, less than $0.01k_BT$ for $0.20<f_O<0.25$ (the compositions where O^{70} is the mesostructural candidate with the lowest free energy).[49] Given these comparable free energies of CSG and O^{70}, the uncertainty in composition measurements, the uncertainty in χ values, and the approximation of perfectly monodisperse blocks, it is not surprising that we experimentally identified CSG as the (presumably) equilibrium mesostructure at compositions where O^{70} has the lowest computed free energy.

The experimental IS(1.06)O blends contain between two and nine neat IS(1.06)O triblock terpolymers. SCFT calculations are performed on model mixtures that mimic these IS(1.06)O blends to compare the predicted and experimental phase behavior and elucidate the molecular factors driving the block copolymer self-assembly. The SCFT inputs contain monodisperse ISO triblocks with the N_i values listed in Table I. The relative quantities of the chains in the model mixtures are equivalent to the relative masses added to the experimental IS(1.06)O blends (values provided in Table SI in the Supporting Information[71]). Accounting for the individual PI or PS block polydispersities is not feasible because of the large quantity of computer memory that would be required for SCFT calculations with that many discrete chain lengths. However, as the blends only differ in the PEO MWDs, approximating the PI and PS blocks as monodisperse should not seriously detract from our efforts to model self-assembly in these materials.

SCFT results obtained for the 11 ISO blends are summarized in Table III. In Table III, the mesostructure with the

TABLE III. Differences in free energy components and relative domain spacings of the morphologies with comparable free energies for the multicomponent ISO blends. All free energies are computed with respect to a reference volume of 118 Å^3 and are normalized by k_BT. In the top half of Table III, all differences (Δ) are listed as the value for CSG minus the value for LAM. In the bottom half of Table III, all differences (Δ) are listed as the value for HEX_O minus the value for CSG.

f_O	PEO PDI	Predicted phase	F_{CSG}-F_{LAM} [a]	ΔF_I [b]	ΔF_O [b]	ΔF_{IS} [c]	ΔF_{SO} [c]	ΔF_{IO} [c]	ΔF_{excess} [d]	d^*_{CSG}/d^*_{LAM} [e]
0.20	1.00	LAM	0.003	−0.063	0.052	0.060	−0.070	0.018	0.006	1.016
0.20	1.17	CSG	–0.025	−0.067	0.057	0.061	−0.093	0.004	0.013	1.028
0.30	1.00	LAM	0.015	−0.040	0.076	0.045	−0.052	0.031	−0.045	1.028
0.30	1.16	CSG	−0.009	−0.040	0.062	0.040	−0.058	0.027	−0.040	1.040
0.30	1.28	CSG	−0.027	−0.039	0.054	0.032	−0.058	0.017	−0.034	1.042
0.30	1.40	CSG	−0.045	−0.036	0.048	0.022	−0.057	0.006	−0.028	1.041
0.33	1.00	LAM	0.026	−0.033	0.079	0.040	−0.040	0.030	−0.050	1.039
0.33	1.27	CSG	−0.012	−0.033	0.053	0.031	−0.045	0.023	−0.041	1.060
0.33	1.30	CSG	−0.017	−0.033	0.051	0.029	−0.045	0.020	−0.039	1.060
0.33	1.45	CSG	−0.043	−0.034	0.036	0.026	−0.051	0.018	−0.038	1.067

f_O	PEO PDI	Predicted phase	F_{HEXo}-F_{CSG} [a]	ΔF_I [b]	ΔF_O [b]	ΔF_{IS} [c]	ΔF_{SO} [c]	ΔF_{IO} [c]	ΔF_{excess} [d]	d^*_{HEXo}/d^*_{CSG} [e]
0.20	1.17	CSG	0.007	−0.031	0.020	0.039	−0.030	0.030	–0.021	1.151
0.20	1.33	HEX_O	−0.003	−0.031	0.017	0.037	−0.033	0.025	–0.018	1.157
0.20	1.46	HEX_O	−0.007	−0.030	0.015	0.035	−0.033	0.023	–0.017	1.159
0.20	1.53	HEX_O	−0.011	−0.030	0.014	0.034	−0.034	0.020	–0.015	1.161
0.30	1.40	CSG	0.002	−0.023	0.032	0.030	−0.026	0.010	–0.021	1.173
0.30	1.73	HEX_O	−0.019	−0.020	0.020	0.016	−0.025	–0.001	–0.009	1.184

[a]Differences in the overall Helmholtz free energy.
[b]Differences in the free energies associated with the conformational entropies of the PI and PEO blocks.
[c]Differences in the interaction energies of PI/PS, PS/PEO, and PI/PEO.
[d]Differences in the excess free energy, a quantity that includes the entropic free energy associated with stretching the PS block and the entropic free energy associated with the localization of chain junction points.
[e]Ratio of the length scales associated with the principal scattering vector ($d^*=2\pi/q^*$).

lowest computed free energy is listed as the "predicted phase" and all of the component free energies are reported as differences (Δ) between the values associated with two mesostructural candidates. The overall Helmholtz free energy for each microstructure can be expressed as the sum of the component free energies according to

$$F_{\text{Helmholtz}} = F_{IS} + F_{SO} + F_{IO} + F_I + F_O + F_{\text{excess}}, \quad (1)$$

where F_{IS}, F_{SO}, and F_{IO} are the free energies associated with PI/PS, PS/PEO, and PI/PEO segment-segment interactions, F_I and F_O are the free energies associated with the conformational entropies of the PI and PEO blocks, and F_{excess} encompasses all other free energy contributions, including the free energies associated with PS chain stretching and the localization of chain junction points. In the top half of Table III, the Δ symbol identifies the quantity associated with CSG minus the quantity associated with LAM. In the lower half of Table III, the Δ symbol indicates the value associated with HEX_O minus the value associated with CSG. Presenting the data in this manner will facilitate the discussion of the thermodynamics underlying the polydispersity-driven morphological transitions.

OOTs from CSG to HEX_O upon heating were identified earlier using experimental data in all of the IS(1.06)O blends with $f_O=0.20$. T_{OOT} depends on the PEO MWD, with increases in PDI_O accompanied by decreases in T_{OOT}. These experimental results indicate that HEX_O becomes more stable (relative to CSG) as PDI_O is increased. The SCFT results also suggest that HEX_O is stabilized by increasing PDI_O; the calculated free energy of the HEX_O morphology decreases below that of the CSG mesostructure as PDI_O is increased from 1.17 to 1.33. Furthermore, the differences in the computed free energies of the CSG and HEX_O morphologies are less than $0.012k_BT$ for all of the ISO blends with $f_O=0.20$, making it unsurprising that OOTs were identified in the experiments.

We believe the thermodynamic driving force for these polydispersity effects is related to the magnitudes of chain stretching summed over the distribution of chain lengths. In all cases the exact contributions to the system free energies depend on the length distribution function of the PEO (and PI and PS) chains.[31] CSG becomes preferred over LAM as the PDI_O is increased from 1.00 to 1.17. According to SCFT, changes in enthalpic interactions are largely responsible for this LAM-to-CSG transition, as both ΔF_{SO} and ΔF_{IO} decrease significantly upon increasing PDI_O. We suggest that these decreases result from a disproportionate increase in the purity of the PEO domain in the CSG morphology, relative to LAM, when PDI_O is raised from 1.00 to 1.17. The composition profiles obtained from SCFT support this reasoning; the purity of the PEO domain in the LAM mesostructure is relatively invariant over this PDI_O range, while the purity of the PEO domain in the CSG morphology increases as PDI_O is increased from 1.00 to 1.17. Presumably the longer PEO chains present in the blend more readily segregate from the PI and PS blocks than do the shorter chains of the monodisperse material.[26] As the PEO MWD is further broadened to $PDI_O=1.33$, HEX_O is predicted to have a lower free energy than CSG. Again the enthalpic interactions favor this transi-

tion, although in a different manner than the LAM to CSG transition described above. As PDI_O is increased from 1.17 to 1.33, ΔF_{IS}, ΔF_{SO}, and ΔF_{IO} all decline by a comparable amount (see bottom half of Table III). We suggest these differences are related to the increase in the d^*_{HEXo}/d^*_{CSG} (where $d^*=2\pi/q^*$) ratio as PDI_O is elevated. The greater increase in d^*_{HEXo} relative to the increase in d^*_{CSG} (as evidenced by the increased d^*_{HEXo}/d^*_{CSG} ratios provided in Table III) means the interfacial area per chain is lower for HEX_O (relative to CSG) at the higher PDI_O value. Consequently, there are fewer segment-segment contacts and lower values of ΔF_{IS}, ΔF_{SO}, and ΔF_{IO}. In addition to enthalpic considerations, the broadening of the PEO MWD relieves the entropic penalty (ΔF_O) incurred by the PEO chains as they stretch to accommodate the HEX_O mesostructure. Presumably the longer chains fill space in the center of the PEO domain, while the shorter chains adopt relaxed conformations near the interface or mix with the PI or PS domains.[26,28,29,34,38,39]

The CSG and HEX_O morphologies were also identified in the IS(1.06)O blends with $f_O=0.30$ and $f_O=0.33$. The SCFT calculations are in good agreement with this experimental analysis and correctly predict the experimentally identified mesostructure (either CSG or HEX_O) for each PEO MWD. [Blend ISO(1.27, 0.33) undergoes an OOT from LAM_3 to CSG upon heating at 210 °C; CSG is the mesostructural candidate with the lowest free energy according to SCFT, with a free energy only $0.026k_BT$ lower than LAM.] Similar arguments to those employed above can be used to describe the thermodynamics driving the phase behavior of these ISO blends with $f_O=0.30$ and $f_O=0.33$. As PDI_O increases above 1, CSG becomes preferred over LAM at both compositions mainly due to (i) a reduction in the entropic penalty (ΔF_O) incurred by the PEO chains as they stretch to accommodate the CSG morphology and (ii) a reduction in the enthalpic interactions (lower ΔF_{IS}, ΔF_{SO}, and ΔF_{IO}) resulting from a decrease in the interfacial area per chain (increased d^*_{CSG}/d^*_{LAM}). These CSG-stabilizing thermodynamic effects may be related to a reduction in packing frustration[82] brought about by the increase in PDI_O.[83] Once the PEO MWD reaches a certain breadth, HEX_O becomes more stable than CSG, as evidenced by the SCFT results (and experimental data) for a blend with $f_O=0.30$ and $PDI_O=1.73$. This CSG-to-HEX_O transition is also largely explained by a combination of (i) and (ii). For all of these blends, polydispersity drives the interfaces to curve toward the polydisperse terminal PEO blocks, a result consistent with previous AB diblock reports.[26–28,30,31]

In addition to the identity of the ordered mesostructure, the T_{ODT} and domain periodicity are important parameters describing block copolymer phase behavior. Our experimental analysis of the effects of PEO block polydispersity on the T_{ODT} is limited by the fact that most of our samples do not disorder below 250 °C (higher temperatures can lead to polymer degradation). Our data do allow for some qualitative analysis of PEO polydispersity effects on T_{ODT} for ISO materials with $f_O=0.20$. Triblock IS(1.06)O(0.20), which contains a narrower PEO MWD than the ISO blends with $f_O=0.20$, disorders at 230 °C. In contrast, none of the ISO blends with this composition disorder below 250 °C, meaning an increase in the PDI of the minority PEO block was accompanied by an increase (of unknown magnitude) in T_{ODT}. This result is consistent with Lynd and Hillmyer's AB diblock report that T_{ODT} increases monotonically with the PDI of a constituent minority block.[40] Our SCFT results also indicate T_{ODT} increases monotonically with the PDI of the PEO block at the compositions probed in this work (as $F_{ordered}-F_{homogeneous}$ decreases as PDI_O increases). We caution against drawing too strong a set of conclusions from our SCFT analysis of T_{ODT}, however, as SCFT fails to qualitatively predict changes in T_{ODT} for all compositions of polydisperse AB diblock copolymers,[28,30,31,40,44] likely because it does not account for fluctuations.[33] While our SCFT analysis qualitatively agrees with our experimental data over the composition range interrogated here, it likely offers limited predictive capability for other compositions.

Polydispersity effects on lattice spacings have been widely studied and, unlike the OOT, there is good general agreement between experiment and theory. Polydispersity has reportedly led to increases in the heights of end-grafted polymer brushes[17] and in the domain periodicities of block copolymers[27–29,31,33,35–37] and block terpolymers[47] in the melt. These increases have been attributed to a reduction in the elastic free energy associated with stretching a polydisperse ensemble of chains compared to its monodisperse counterpart.[28,30,31] The effects of PEO polydispersity on ISO domain periodicities are summarized in Fig. 8, where the measured and predicted normalized principal scattering lengths ($d^*=2\pi/q^*$) are plotted as a function of PDI_O for the ISO materials with $f_O=0.20$, 0.30, and 0.33. The data are presented in this normalized manner to facilitate quantitative comparison of the experiment and theory; SCFT does not typically accurately predict absolute domain periodicities using χ values measured at phase transitions.[43] The normalized SCFT predictions are in good qualitative agreement with the experimental data, with the normalized d^* values increasing monotonically with the polydispersity of the terminal PEO block. This result generally agrees with previous block copolymer[27–29,31,35–37] and block terpolymer[47] reports; presumably the polydispersity relieves the entropic free energy penalty associated with stretching the PEO chains and leads to larger lattice spacings. Interestingly, our SCFT predictions corroborate the experimental conclusion that the sensitivity of the lattice spacing to changes in PDI is higher at increased segregation strengths (i.e., an increase in PDI_O for the materials with $f_O=0.33$ leads to a bigger relative increase in domain periodicity than an equivalent increase in PDI_O does for the samples with $f_O=0.20$). This trend was not predicted by several SCFT analyses of polydisperse AB diblock copolymers,[28,29,31] although it was identified experimentally by Lynd and Hillmyer[27] for polydisperse poly[(ethylene-*alt*-propylene)-*b*-(DL-lactide)] diblock copolymers. There are, however, some quantitative differences between our ISO experimental data and SCFT results. Namely, the SCFT consistently overestimates the relative increase in d^*. There are numerous potential sources of this discrepancy between experiment and theory, including uncertainties in measurements of χ and N, the approximation of the PI and PS blocks as monodisperse, and nonequilibrium

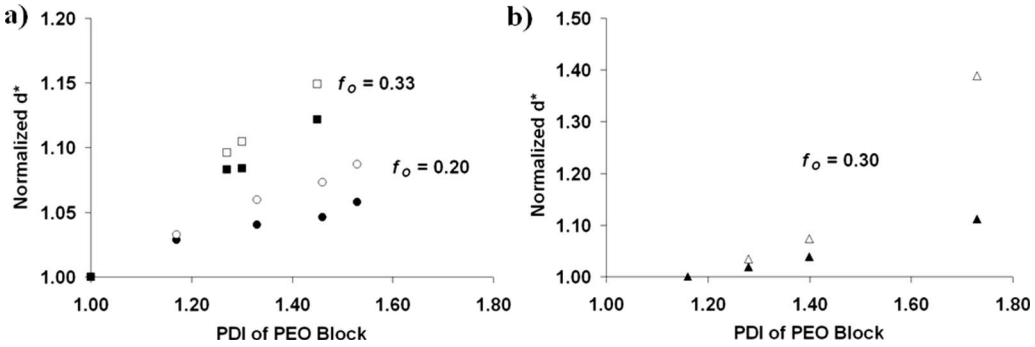

FIG. 8. Measured (by SAXS, solid points) and predicted (by SCFT, open points) normalized d^* values ($d^*=2\pi/q^*$) for the ISO samples with (a) $f_O=0.20$, 0.33 and (b) $f_O=0.30$. The experimentally measured principal scattering lengths are normalized by dividing them by d^* measured for triblock IS(1.06)O(0.20) (data for $f_O=0.20$), triblock IS(1.06)O(0.33) (data for $f_O=0.33$), or blend ISO(1.16, 0.30) (data for $f_O=0.30$). Here PDI_O is approximated as 1 for samples IS(1.06)O(0.20) and IS(1.06)O(0.33). The predicted d^* values are normalized by dividing them by either d^* computed for monodisperse ISO triblocks with the same composition ($f_O=0.20,0.33$) or by d^* calculated for blend ISO(1.16, 0.30) ($f_O=0.30$). In all cases d^* was computed for the morphology identified using experimental data, even if it was not the mesostructure with the lowest calculated free energy [e.g., the predicted d^* for blend ISO(1.46, 0.20) was computed for the CSG morphology, not HEX_O].

effects (our experimental materials may not be fully equilibrated following the relatively short annealing times). Further experimental and theoretical investigations are required to fully understand polydispersity effects on lattice spacings.

C. IS(1.16, 1.31, 1.44)O free energy calculations

The computed free energies (relative to LAM and normalized by k_BT) of the morphological candidates in the model systems designed to mimic the IS(1.16)O, IS(1.31)O, and IS(1.44)O materials are provided in Fig. 9. The solid curves represent the free energies of the morphologies in the model polydisperse systems, while the dashed lines, for comparison, correspond to the free energies of the mesostructures in monodisperse systems with the same molecular weights and compositions. The free energy curves for the HEX_I, HEX_O, CSG, O^{70}, and LAM morphologies are provided for the model IS(1.16)O system in the upper left plot. The HEX_I and HEX_O mesostructures do not closely compete for the lowest free energy in this or any other system summarized in Fig. 9. As a result, the other three plots only include the CSG, O^{70}, and LAM free energies to facilitate analysis of these closely competing mesostructural candidates.

The monodisperse and polydisperse free energy curves provided in the IS(1.16)O plots in the upper half of Fig. 9 correspond to model monodisperse and polydisperse systems that approximate the experimental IS(1.06)O and IS(1.16)O

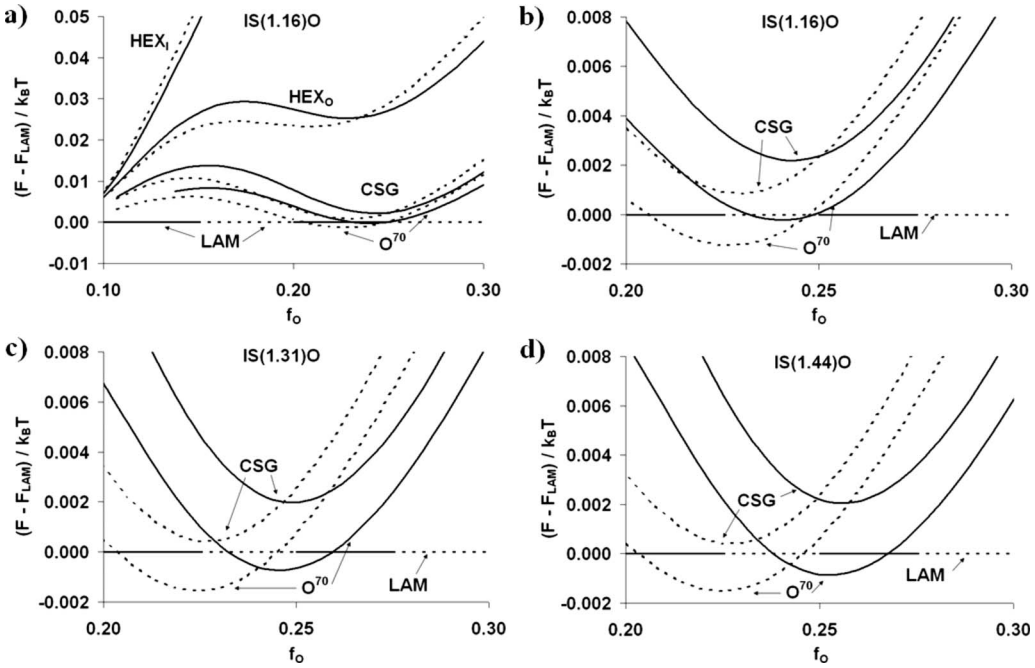

FIG. 9. Calculated SCFT free energies (relative to LAM and normalized by k_BT) of competing mesostructural candidates for model systems that approximate the experimental [(a) and (b)] IS(1.16)O, (c) IS(1.31)O, and (d) IS(1.44)O systems. All of the free energy curves were computed at the molecular weights and along the isopleths defined by the number-averaged N_I and N_S values that are listed in Table I. The HEX_I and HEX_O morphologies have higher computed free energies for all of the systems and, for clarity, their free energy curves are not provided on the (b) IS(1.16)O, (c) IS(1.31)O, and (d) IS(1.44)O plots. The solid lines are the curves computed for the polydisperse materials, while the dashed lines are calculated for monodisperse systems with the same compositions and molecular weights.

materials, respectively. As discussed above, SCFT predicts a morphology sequence of LAM→O^{70}→LAM upon increasing f_O for the monodisperse materials, while the LAM →CSG→O^{70}→LAM sequence was identified in the IS(1.06)O polymers. As the PS MWD is broadened to a PS PDI=1.16, SCFT predicts that both the O^{70} and CSG mesostructures increase in free energy relative to the LAM morphology. O^{70} still, however, has the lowest computed free energy over a narrow composition range ($0.23<f_O<0.25$). This predicted LAM→O^{70}→LAM sequence was identified using the experimental data obtained for the IS(1.16)O samples, although the experimental network window ($0.11<f_O<0.25$) is significantly wider than predicted. The IS(1.06)O and IS(1.16)O characterization data indicate that increasing the PS PDI from 1.06 to 1.16 changes the identity of the predominant network structure from CSG to O^{70}. This result intimates that O^{70} becomes lower in free energy, relative to CSG, in this composition range ($0.10<f_O<0.25$) as the PS PDI increases from 1.06 to 1.16. The SCFT calculations agree with this deduction, as the calculated free energy of O^{70} (relative to CSG) is lower in the model IS(1.16)O system than in the monodisperse system when $0.15<f_O<0.27$ (see Fig. S2 in the Supporting Information[71] for details).

The SCFT analysis for the model IS(1.31)O system indicates that O^{70} is the lowest free energy mesostructural candidate at higher f_O and over a narrower composition range ($0.24<f_O<0.26$ versus $0.21<f_O<0.25$) in the IS(1.31)O polymers than it is in monodisperse materials with the same molecular weights and compositions. We did not identify O^{70} (or CSG) in the experimental materials. It is possible that the network window occupies compositions not investigated experimentally; network structures could form in either the $0.11<f_O<0.14$ or $0.17<f_O<0.24$ composition ranges. It should also be noted that the calculated free energy differences between LAM, CSG, and O^{70} are small ($<0.006k_BT$) over the computed network window. Uncertainties in composition measurements, molecular weights, and χ values or the block polydispersity approximations (monodisperse PI and PEO blocks, a PS chain distribution comprised of only 13 different chain lengths) could cause SCFT to erroneously identify the lowest free energy mesostructural candidate.

SCFT analysis also suggests that the O^{70} window will narrow and shift to higher PEO volume fractions (from $0.21<f_O<0.25$ to $0.24<f_O<0.27$) as the PS PDI is increased from 1 to 1.44 [as shown in the IS(1.44)O plot in Fig. 9(d)]. Unlike the IS(1.31)O experimental data, the IS(1.44)O data are in qualitative agreement with the prediction that the network window shifts to higher PEO volume fractions. A network window was identified in the IS(1.44)O materials beginning at $f_O=0.17$, while it begins in the $0.10<f_O<0.13$ range in comparable monodisperse materials [e.g., the IS(1.06) series or the ISO polymers characterized in Refs. 50–52]. The experimental data are also consistent with the SCFT calculations that indicate the LAM, CSG, and O^{70} mesostructures have comparable free energies (they differ by $<0.006k_BT$ in the network window); all three of these morphologies were identified in the experimental materials. We did not prepare any LAM-forming IS(1.44)O materials on the PEO-rich side of the network window and are thus unable to evaluate the SCFT prediction that the window would narrow.

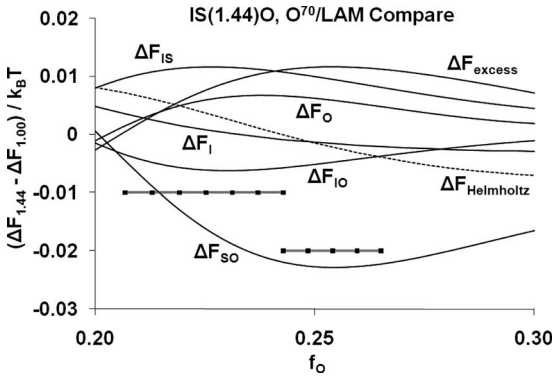

FIG. 10. Differences in computed free energy components (normalized by k_BT) of the O^{70} and LAM morphologies between the model IS(1.44)O system and its monodisperse counterpart. The values plotted on the ordinate are obtained by (i) subtracting the value of each free energy component calculated for LAM from the value of each component computed for O^{70} (i.e., $\Delta F_i=F_{i,O70}-F_{i,LAM}$) and (ii) subtracting these component differences for a PS PDI=1.00 from these component differences for a PS PDI=1.44. The solid curves represent the components of the free energies and are labeled using the nomenclature described in Table III. The dashed curve represents the overall Helmholtz free energy. The horizontal lines at ordinate values of −0.01 and −0.02 (marked with ■) connote the compositions at which SCFT predicts O^{70} to be the equilibrium mesostructure for the monodisperse ($0.21<f_O<0.25$) and polydisperse ($0.24<f_O<0.27$) systems, respectively.

To understand the thermodynamics underlying these polydispersity effects, we can examine the components of the free energies computed using SCFT. In our three systems, the trends in the component free energy differences between the network morphologies and LAM are qualitatively similar; we provide representative differences comparing LAM and O^{70} for the IS(1.44)O system and its monodisperse counterpart in Fig. 10. The data are plotted such that negative values indicate a preference for O^{70} at PS PDI=1.44, while positive values denote a predilection for LAM at this elevated PS PDI. The thermodynamic factors that drive network formation at higher f_O values for PS PDI=1.44 are the free energies associated with the conformational entropy of the PI block (ΔF_I) and the PS/PEO and PI/PEO segment-segment interactions (ΔF_{SO} and ΔF_{IO}, respectively). The free energies that favor LAM in this composition window ($0.24<f_O<0.27$) are those associated with the PI/PS segment-segment interactions (ΔF_{IS}), the conformational entropy of the PEO chains (ΔF_O), and the excess entropy (ΔF_{excess}), which includes the conformational entropy of the PS segments and the localization of chain junctions. We suggest that these thermodynamic changes are driven by changes in the segment density distributions within the unit cells. The composition profiles computed by SCFT indicate that increases in the PS polydispersity are accompanied by additional mixing among all of the block segments (i.e., decreases in domain purities). While the broadening of the PS MWD decreases domain purities in both the LAM and O^{70} mesostructures, the relative changes in each domain are mesostructure dependent. The number of contacts between PEO segments and both the PI and PS chains increases to a larger extent in the LAM morphology than it does in the O^{70} me-

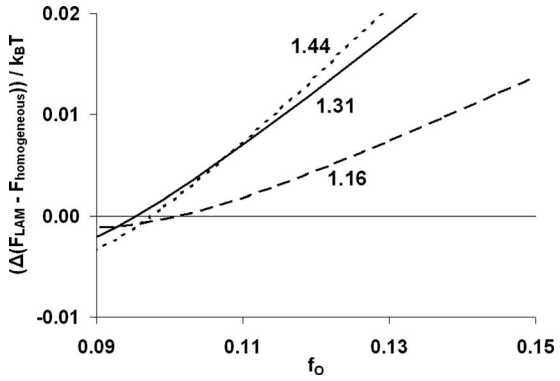

FIG. 11. Curves representing the relative stability of the LAM mesostructure relative to a homogeneous, disordered state for the polydisperse systems, and their monodisperse analogs. The values plotted on the ordinate were obtained by (i) computing $F_{\mathrm{LAM}}-F_{\mathrm{homogeneous}}$ for both the monodisperse and polydisperse systems and (ii) subtracting this difference for the monodisperse system from this difference for the polydisperse system (e.g., $\Delta F_{1.44}-\Delta F_{1.00}$). When the ordinate value is negative, LAM is more stable for the polydisperse material (i.e., higher T_{ODT} for the polydisperse systems). When the ordinate value is positive, LAM is more stable for the monodisperse material (i.e., lower T_{ODT} for the polydisperse systems).

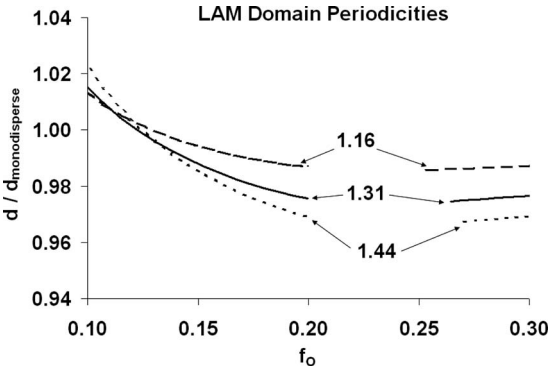

FIG. 12. Normalized LAM domain periodicities computed using SCFT for the three polydisperse ISO systems. The values are normalized by dividing them by the lattice spacings calculated for the monodisperse analogs to the polydisperse series. Results are only plotted when SCFT predicts LAM to be the equilibrium mesostructure for both the monodisperse and polydisperse systems; the gaps represent compositions at which O^{70} is predicted to be the equilibrium morphology for the polydisperse and/or monodisperse materials.

sostructure when PS PDI increases from 1 to 1.44, making ΔF_{SO} and ΔF_{IO} negative in Fig. 10. The increases in the PI/PS contacts, in contrast, are more significant in O^{70} than in LAM, rendering ΔF_{IS} positive in Fig. 10. The net effects of the increased PS PDI on the ISO phase behavior are subtle and cannot be rationalized using the phenomenological explanation that increases in block PDI lead to a preference for mesostructures with domain interfaces curved toward the polydisperse domain. These bridged PS block PDI effects are qualitatively different than those associated with an increase in the terminal PEO block polydispersity and are not consistent with previous studies[26–28,30,31] of AB block copolymer systems.

Changing PS polydispersity also alters T_{ODT} and domain periodicity. Unfortunately, no firm conclusions regarding the effects of PS polydispersity on T_{ODT} can be drawn from the experimental data. A plot of the measured T_{ODT} values versus f_O (values from Table I, plot not shown) for each PS PDI value yields a scatter of points that generally lie on the same line, with the exception of the IS(1.31)O values, which are slightly below those of the other materials. Given the lack of clear trends and the molecular weight and composition variations across the parent IS diblocks (and thus the ISO triblocks), it is not possible to say whether the differences in the T_{ODT} values are driven by changes in the PS MWD. Unlike with the PEO polydispersity, SCFT does not predict T_{ODT} to increase monotonically with PS polydispersity. A plot describing the stability of LAM relative to the disordered state in the polydisperse ISO systems and their monodisperse analogs is provided in Fig. 11. For the low f_O values, the PS polydispersity stabilizes the ordered LAM mesostructure relative to the homogeneous, disordered state (ordinate values below 0), a result qualitatively similar to the SCFT analysis of the PEO polydispersity. However, as f_O increases, F_{LAM} approaches and then surpasses $F_{\mathrm{homogeneous}}$ (ordinate values above 0) for the polydisperse systems, representing a polydispersity-induced destabilization of the ordered mesostructure (i.e., a decrease in T_{ODT}). Note that while LAM SCFT results are plotted in Fig. 11, the same trend is present in the calculations for the other morphological candidates. While the scatter in the experimental data prevents us from evaluating the validity of these predictions, this analysis does provide a rationale for polydispersity-driven decreases in T_{ODT} within the SCFT framework. SCFT generally predicts that T_{ODT} should increase monotonically with block PDI for AB diblock copolymers,[28] and only a few previous theoretical treatments predicted that T_{ODT} could decrease with an increase in block PDI.[30,33] Matsen[30] considered the close-packed spherical morphology in his SCFT investigation of AB diblock copolymers and predicted polydispersity-driven decreases in T_{ODT} at some compositions. Beardsley and Matsen[33] studied polydisperse AB diblocks using lattice-based Monte Carlo simulations and predicted that T_{ODT} could decrease slightly with increasing block PDI for symmetric diblocks. They suggested that their simulations contradicted SCFT results because the latter method does not consider fluctuations.[33]

The domain periodicities measured using SAXS, like the experimental T_{ODT} data, do not follow any clear trends with PS polydispersity. We can, however, compute the predicted polydispersity-driven changes in lattice spacings using SCFT. These results are provided in Fig. 12 for compositions where LAM is the lowest free energy mesostructural candidate for both the polydisperse and monodisperse materials. (Presenting the results in this manner eliminates discontinuities in the curves resulting from morphological transitions. Domain periodicities computed when O^{70} is the lowest free energy mesostructural candidate follow the same general trends illustrated in Fig. 12.) In this plot the calculated domain periodicities of the polydisperse series are normalized by dividing them by the values computed for the monodisperse analogs. SCFT predicts that, for low values of f_O ($f_O < \sim 0.12$ in Fig. 12), the LAM domain periodicity increases slightly with the PS PDI, while for higher values of f_O, the LAM lattice spacing decreases with increasing PS PDI. The

predicted variations in domain spacing are small, making it unsurprising that no trends were identified in the experimental data.

Increasing the polydispersity of the middle PS block does not lead to the same qualitative morphological changes as increasing the polydispersity of the terminal PEO block. Broadening the PEO MWD resulted in changes that generally mirrored those reported in polydisperse AB diblock copolymers—namely, interfaces tended to curve toward the polydisperse block and domain periodicity increased monotonically with block polydispersity.[44] Increases in the PS block polydispersity did not lead to these same trends, as the morphological changes depended on the block terpolymer composition. We attribute these differences to the fact that the middle PS block does not have any dangling chain ends, but is covalently bonded to both PI and PEO chains. The enthalpic incompatibility between these terminal PI and PEO blocks (χ_{IO}=0.183 at 100 °C)[80] prevents the polydisperse PS chains from behaving like the polydisperse chains in AB diblock or ABA triblock copolymers; the short PS chains do not simply adopt relaxed conformations near the domain interface and the long chains do not always occupy space in the center of the domain. Generally, the effects of polydispersity in blocks without free chain ends will depend not only on the chain distribution functions but also the sequence of χ values in a given system. This paper provides some foundation for analyzing these complicated polydisperse systems.

V. CONCLUSIONS

The effects of middle PS or terminal PEO block polydispersity on the phase behavior of ISO triblock terpolymers with $f_I \approx f_S$ have been probed both experimentally and theoretically. The different block polydispersities drive different changes in ISO phase behavior. The terminal PEO block polydispersity effects generally mimic polydispersity effects reported in AB diblock or ABA triblock copolymers,[44] and there is qualitative agreement between our experimental and SCFT results for the ISO system. Namely, lattice periodicities increase monotonically with PEO block polydispersity and morphologies with interfaces curved toward the polydisperse PEO block are preferred. Broadening the PS MWD does not lead to the same general trends in ISO triblock terpolymers as an increase in PEO polydispersity. Increases in PS polydispersity do not always lead to increases in domain periodicity and do not always drive interfaces to curve toward the polydisperse block. These differences are attributed to the fact that, unlike the polydisperse PEO chains and the polydisperse blocks in AB block copolymers, the polydisperse PS chains are covalently connected to two enthalpically incompatible blocks and forced to adopt conformations that bridge the domain. The exact effects of middle block polydispersity will depend on both the chain distribution functions and the sequence of χ parameters.

Notably, in the ISO system, neither PS nor PEO block polydispersities prevent the formation of the multiply continuous CSG and/or O^{70} network mesostructures, although the compositions at which both are stable vary with block MWDs. We have used terminal PEO block polydispersity (introduced by multicomponent blending) to drive a morphological transition from LAM to the CSG network mesostructure, effectively widening the network window. These results highlight the utility of polydispersity as a tool to tune block terpolymer phase behavior.[62,63]

ACKNOWLEDGMENTS

The authors gratefully acknowledge financial support from the Department of Energy through Grant No. 5-35908 and through a subcontract to UT-Battelle (Grant No. 4000041622). We also acknowledge support from the National Science Foundation (Grant No. NSF DMR–0704192). Graduate fellowships to A.J.M. from the Department of Homeland Security and the Department of Defense are gratefully acknowledged. Portions of this work were performed at the DuPont-Northwestern-Dow Collaborative Access Team (DND-CAT) located at Sector 5 of the Advanced Photon Source (APS). DND-CAT is supported by E.I. DuPont de Nemours and Co., The Dow Chemical Company, and the State of Illinois. Use of the Advanced Photon Source (APS) was supported by the U.S. Department of Energy, Office of Science, Office of Basic Energy Sciences, under Contract No. DE-AC02-06CH11357. We thank Professor David C. Morse for providing his group's SCFT code and thank Professor Thomas R. Hoye for use of his group's ozonolysis equipment.

[1] G. Holden, N. R. Legge, R. P. Quirk, and H. E. Schroeder, *Thermoplastic Elastomers*, 2nd ed. (Hansen, New York, 1996).
[2] S. Perrier and X. Wang, Nature (London) **445**, 271 (2007).
[3] D. J. Arriola, E. M. Carnahan, P. D. Hustad, R. L. Kuhlman, and T. T. Wenzel, Science **312**, 714 (2006).
[4] M. Zintl and B. Rieger, Angew. Chem., Int. Ed. **46**, 333 (2007).
[5] C. W. Bielawski and R. H. Grubbs, Prog. Polym. Sci. **32**, 1 (2007).
[6] C. J. Hawker, A. W. Bosman, and E. Harth, Chem. Rev. (Washington, D.C.) **101**, 3661 (2001).
[7] M. Kamigaito, T. Ando, and M. Sawamoto, Chem. Rev. (Washington, D.C.) **101**, 3689 (2001).
[8] K. Matyjaszewski and J. Xia, Chem. Rev. (Washington, D.C.) **101**, 2921 (2001).
[9] W. A. Braunecker and K. Matyjaszewski, Prog. Polym. Sci. **32**, 93 (2007).
[10] D. Bendejacq, V. Ponsinet, M. Joanicot, Y.-L. Loo, and R. A. Register, Macromolecules **35**, 6645 (2002).
[11] A.-V. Ruzette, S. Tence-Girault, L. Leibler, F. Chauvin, D. Bertin, O. Guerret, and P. Gerard, Macromolecules **39**, 5804 (2006).
[12] L. Leibler, Macromolecules **13**, 1602 (1980).
[13] L. Leibler and H. Benoit, Polymer **22**, 195 (1981).
[14] G. Hadziioannou and A. Skoulios, Macromolecules **15**, 267 (1982).
[15] K. M. Hong and J. Noolandi, Polym. Commun. **25**, 265 (1984).
[16] H. Benoit and G. Hadziioannou, Macromolecules **21**, 1449 (1988).
[17] S. T. Milner, T. A. Witten, and M. E. Cates, Macromolecules **22**, 853 (1989).
[18] C. Burger, W. Ruland, and A. N. Semenov, Macromolecules **23**, 3339 (1990).
[19] K. Almdal, J. H. Rosedale, and F. S. Bates, Macromolecules **23**, 4336 (1990).
[20] R. J. Spontak and M. C. Williams, J. Polym. Sci., Part B: Polym. Phys. **28**, 1379 (1990).
[21] D. Nguyen, X. Zhong, C. E. Williams, and A. Eisenberg, Macromolecules **27**, 5173 (1994).
[22] I. Erukhimovich and A. V. Dobrynin, Macromol. Symp. **81**, 253 (1994).
[23] A. V. Dobrynin and L. Leibler, Macromolecules **30**, 4756 (1997).
[24] H. J. Angerman, G. ten Brinke, and J. J. M. Slot, Eur. Phys. J. B **12**, 397 (1999).
[25] M. Foroutan and M. A. Jafarizadeh, Physica A **329**, 337 (2003).

[26] S. W. Sides and G. H. Fredrickson, J. Chem. Phys. **121**, 4974 (2004).
[27] N. A. Lynd and M. A. Hillmyer, Macromolecules **38**, 8803 (2005).
[28] D. M. Cooke and A.-C. Shi, Macromolecules **39**, 6661 (2006).
[29] M. W. Matsen, Eur. Phys. J. E **21**, 199 (2006).
[30] M. W. Matsen, Phys. Rev. Lett. **99**, 148304 (2007).
[31] N. A. Lynd, M. A. Hillmyer, and M. W. Matsen, Macromolecules **41**, 4531 (2008).
[32] Y. Han, J. Cui, and W. Jiang, Macromolecules **41**, 6239 (2008).
[33] T. M. Beardsley and M. W. Matsen, Eur. Phys. J. E **27**, 323 (2008).
[34] A. Soldera, Y. Qi and W. T. Capehart, J. Chem. Phys. **130**, 064902 (2009).
[35] Y. Matsushita, A. Noro, M. Iinuma, J. Suzuki, H. Ohtani, and A. Takano, Macromolecules **36**, 8074 (2003).
[36] A. Noro, M. Iinuma, J. Suzuki, A. Takano, and Y. Matsushita, Macromolecules **37**, 3804 (2004).
[37] A. Noro, D. Cho, A. Takano, and Y. Matsushita, Macromolecules **38**, 4371 (2005).
[38] A. Noro, M. Okuda, F. Odamaki, D. Kawaguchi, N. Torikai, A. Takano, and Y. Matsushita, Macromolecules **39**, 7654 (2006).
[39] N. Torikai, A. Noro, M. Okuda, F. Odamaki, D. Kawaguchi, A. Takano, and Y. Matsushita, Physica B **385-386**, 709 (2006).
[40] N. A. Lynd and M. A. Hillmyer, Macromolecules **40**, 8050 (2007).
[41] N. A. Lynd, B. D. Hamilton, and M. A. Hillmyer, J. Polym. Sci., Part B: Polym. Phys. **45**, 3386 (2007).
[42] J. Listak, W. Jakubowski, L. Mueller, A. Plichta, K. Matyjaszewski, and M. R. Bockstaller, Macromolecules **41**, 5919 (2008).
[43] C. J. Ellison, A. J. Meuler, J. Qian, C. M. Evans, L. M. Wolf, and F. S. Bates, J. Phys. Chem. B **113**, 3726 (2009).
[44] N. A. Lynd, A. J. Meuler, and M. A. Hillmyer, Prog. Polym. Sci. **33**, 875 (2008).
[45] D. A. Hajduk, H. Takenouchi, M. A. Hillmyer, F. S. Bates, M. E. Vigild, and K. Almdal, Macromolecules **30**, 3788 (1997).
[46] E. W. Cochran, C. J. Garcia-Cervera, and G. H. Fredrickson, Macromolecules **39**, 2449 (2006).
[47] Y. Jiang, X. Yan, H. Liang, and A.-C. Shi, J. Phys. Chem. B **109**, 21047 (2005).
[48] A. J. Meuler, C. J. Ellison, C. M. Evans, M. A. Hillmyer, and F. S. Bates, Macromolecules **40**, 7072 (2007).
[49] A. J. Meuler, C. J. Ellison, M. A. Hillmyer, and F. S. Bates, Macromolecules **41**, 6272 (2008).
[50] T. S. Bailey, C. M. Hardy, T. H. Epps III, and F. S. Bates, Macromolecules **35**, 7007 (2002).
[51] T. H. Epps III, E. W. Cochran, C. M. Hardy, T. S. Bailey, R. S. Waletzko, and F. S. Bates, Macromolecules **37**, 7085 (2004).
[52] T. H. Epps III, E. W. Cochran, T. S. Bailey, R. S. Waletzko, C. M. Hardy, and F. S. Bates, Macromolecules **37**, 8325 (2004).
[53] B. J. Dair, C. C. Honeker, D. B. Alward, A. Avgeropoulos, N. Hadjichristidis, L. J. Fetters, M. Capel, and E. L. Thomas, Macromolecules **32**, 8145 (1999).
[54] B. J. Dair, A. Avgeropoulos, N. Hadjichristidis, and E. L. Thomas, J. Mater. Sci. **35**, 5207 (2000).
[55] A. J. Meuler, G. Fleury, M. A. Hillmyer, and F. S. Bates, Macromolecules **41**, 5809 (2008).
[56] T. Hashimoto, K. Tsutsumi, and Y. Funaki, Langmuir **13**, 6869 (1997).
[57] A. M. Urbas, M. Maldovan, P. DeRege, and E. L. Thomas, Adv. Mater. (Weinheim, Ger.) **14**, 1850 (2002).
[58] E. J. W. Crossland, M. Kamperman, M. Nedelcu, C. Ducati, U. Wiesner, D. Smilgies, G. E. S. Toombes, M. A. Hillmyer, S. Ludwigs, U. Steiner, and H. J. Snaith, Nano Lett. (unpublished).
[59] E. J. W. Crossland, M. Nedelcu, C. Ducati, S. Ludwigs, M. A. Hillmyer, U. Steiner, and H. J. Snaith, Nano Lett. (unpublished).
[60] V. Z.-H. Chan, J. Hoffman, V. Y. Lee, H. Latrou, A. Avgeropoulos, N. Hadjichristidis, R. D. Miller, and E. L. Thomas, Science **286**, 1716 (1999).
[61] T. Hahn, *International Tables for Crystallography*, 4th ed. (Kluwer Academic, Boston, 1994), Vol. A.
[62] L. Leibler, Prog. Polym. Sci. **30**, 898 (2005).
[63] M. A. Hillmyer, J. Polym. Sci., Part B: Polym. Phys. **45**, 3249 (2007).
[64] S. Ndoni, C. M. Papadakis, F. S. Bates, and K. Almdal, Rev. Sci. Instrum. **66**, 1090 (1995).
[65] A. B. Pangborn, M. A. Giardello, R. H. Grubbs, R. K. Rosen, and F. J. Timmers, Organometallics **15**, 1518 (1996).
[66] T. S. Bailey, H. D. Pham, and F. S. Bates, Macromolecules **34**, 6994 (2001).
[67] A. J. Meuler, M. K. Mahanthappa, M. A. Hillmyer, and F. S. Bates, Macromolecules **40**, 760 (2007).
[68] M. A. Hillmyer and F. S. Bates, Macromolecules **29**, 6994 (1996).
[69] L. J. Fetters, D. J. Lohse, D. Richter, T. A. Witten, and A. Zirkel, Macromolecules **27**, 4639 (1994).
[70] J. H. Rosedale and F. S. Bates, Macromolecules **23**, 2329 (1990).
[71] See EPAPS Document No. E-JCPSA6-130-057921 for (a) Table S1, a list of the relative mass fractions of the neat IS(1.06)O triblocks in each IS(1.06) blend, (b) Fig. S1, a plot of the isochronal G' measurements obtained from specimen IS(1.06)O(0.20), (c) Fig. S2, the SAXS data acquired for samples IS(1.16)O(0.13) and IS(1.16)O(0.15), (d) Fig. S3, the isochronal G' and SAXS data acquired for specimen IS(1.44)O(0.21), (e) Fig. S4, comparisons between the PS block MWDs measured using SEC and the multimodal blends used as inputs for the SCFT calculations for the IS(1.16)O, IS(1.31)O, and IS(1.44)O systems, and (f) Fig. S5, a plot containing curves that represent the differences in the SCFT free energies of the CSG and O^{70} mesostructures for monodisperse ISO and polydisperse IS(1.16)O materials. For more information on EPAPS, see http://www.aip.org/pubservs/epaps.html.
[72] C. A. Tyler, J. Qin, F. S. Bates, and D. C. Morse, Macromolecules **40**, 4654 (2007).
[73] H. Mao and M. A. Hillmyer, Soft Matter **2**, 57 (2006).
[74] M. W. Matsen, J. Phys.: Condens. Matter **14**, R21 (2002).
[75] G. H. Fredrickson, *The Equilibrium Theory of Inhomogeneous Polymers* (Oxford University Press, New York, 2006).
[76] M. W. Matsen, J. Chem. Phys. **108**, 785 (1998).
[77] C. A. Tyler and D. C. Morse, Phys. Rev. Lett. **94**, 208302 (2005).
[78] C. A. Tyler and D. C. Morse, Macromolecules **36**, 8184 (2003).
[79] The SCFT code is available on the internet at http://www.cems.umn.edu/research/morse/code/pscf/home.php.
[80] H. Frielinghaus, N. Hermsdorf, K. Almdal, K. Mortensen, L. Messe, L. Corvazier, J. P. A. Fairclough, A. J. Ryan, P. D. Olmsted, and I. W. Hamley, Europhys. Lett. **53**, 680 (2001).
[81] E. W. Cochran, D. C. Morse, and F. S. Bates, Macromolecules **36**, 782 (2003).
[82] M. W. Matsen and F. S. Bates, Macromolecules **29**, 7641 (1996).
[83] F. J. Martínez-Veracoechea and F. A. Escobedo, Macromolecules **38**, 8522 (2005).